https://doi.org/10.5194/essd-2025-628
Preprint. Discussion started: 24 March 2026

Open Access Earth System Science Data Discussions

iDust-ut: A Global Wind Erosion Threshold Dataset for Enhanced Dust Forecasting

Mei Chong[1,2], Shengkai Wang[3], Xi Chen[1*], Yuan Liang[4], Bing Pu[5], Shian-Jiann Lin[4], Zhi Liang[4], and Yimin Liu[1,2]

[1]State Key Laboratory of Earth System Numerical Modeling and Application, Institute of Atmospheric Physics, Chinese Academy of Sciences, Beijing, China
[2]University of Chinese Academy of Sciences, Beijing, China
[3]Xiamen University, Xiamen, China
[4]TianJi Weather Science and Technology Company, Beijing, China
[5]Department of Geography and Atmospheric Science, University of Kansas, Lawrence, Kansas

Correspondence to: Xi Chen (chenxi@lasg.iap.ac.cn)

Abstract. Accurate global dust forecasting is essential for public health, transportation safety, and industry operations. Current models underestimate extreme dust events with pronounced regional biases, primarily due to poor parameterization of the wind erosion threshold (u_t), a fundamental parameter representing the minimum wind speed for dust emission initiation. This study develops iDust-ut, an advanced global threshold dataset through a multi-source data fusion approach that integrates ground observations, satellite remote sensing, and multiple reanalysis datasets. Validation against independent field observations demonstrates high accuracy, with a correlation coefficient of 0.93 and a mean absolute error of 0.8 m s^{-1}, far outperforming existing products. Additionally, this study introduces a model-adaptive threshold adjustment scheme that compensates for systematic wind speed biases across different numerical models. Based on annual 2023 evaluations across Northwestern China (for PM_{10}) and global dust belt regions (for dust optical depth), implementation of the iDust-ut dataset with adaptive adjustment substantially enhances forecast performance of the iDust model compared to the approach of using a global constant threshold. Specifically, the Threat Score for extreme PM_{10} forecasting in Northwestern China increased by 108 % (from 17.39 % to 36.25 %), while the Threat Score for extreme dust optical depth simulation in global dust belt regions improved by 47 %. The enhanced model performance substantially outperforms the European Centre for Medium-Range Weather Forecasts (ECMWF) operational aerosol forecasts in many key metrics. The iDust-ut dataset offers an immediately deployable, computationally efficient solution for enhancing dust forecasting accuracy across various modeling systems. The iDust-ut dataset can be freely accessed via https://zenodo.org/doi/10.5281/zenodo.15580883 (Chong and Chen, 2026).

https://doi.org/10.5194/essd-2025-628
Preprint. Discussion started: 24 March 2026

Open Access Earth System Science Data Discussions

Key Words: Wind erosion threshold; Multi-source data fusion; Dust forecasting; Extreme dust events; Wind speed bias; iDust

1 Introduction

Mineral dust aerosols profoundly affect global climate dynamics, regional air quality, and critical socioeconomic sectors worldwide. Accurate dust forecasting has become increasingly vital for multiple applications: aviation operations require precise dust predictions to prevent engine damage and visibility hazards that threaten flight safety (Scherllin-Pirscher et al., 2025); public health systems depend on reliable dust warnings to protect vulnerable populations from respiratory impacts and to reduce exposure-related mortality (Zhang et al., 2023); the rapidly expanding renewable energy sector relies on dust forecasts to anticipate efficiency losses from solar radiation scattering and panel contamination, enabling optimized maintenance scheduling and power generation planning (IEA, 2024; Masoom et al., 2021; Panat and Varanasi, 2022).

Despite this critical demand, current operational dust forecasting systems exhibit significant performance limitations. Leading systems such as the European Centre for Medium-Range Weather Forecasts Copernicus Atmosphere Monitoring Service (ECMWF-CAMS; Rémy et al., 2019, 2022) and the recently developed global dust-weather integrated model, iDust (Chen et al., 2025), tend to underestimate extreme dust events and exhibit pronounced spatial imbalances, overestimating dust in certain regions while substantially underestimating activity in others (Pitkänen et al., 2023; Chen et al., 2025). The fundamental challenge underlying these limitations lies in the inadequate parameterization of dust emission processes, particularly the uncertainty in the wind erosion threshold (u_t), the minimum wind speed required to initiate dust particle mobilization from surface sources**.** This threshold serves as the primary control mechanism for dust emission in numerical models (e.g., Ginoux et al., 2001; Darmenova et al., 2009; Leung et al., 2023; Hennen et al., 2024). The accurate estimation of u_t faces substantial scientific challenges due to its complex dependence on multiple environmental factors, including soil composition, particle size distribution, vegetation coverage, surface moisture, and terrain roughness (Yang et al., 2017; Kong et al., 2021).

Existing approaches for u_t determination fall into three primary categories, each with significant limitations. Direct field measurements (Stout and Arimoto, 2010; Nelli et al., 2024) provide the most reliable u_t estimates. However, their sparse spatial coverage and high operational costs make them unsuitable for constructing global datasets required by operational forecasting systems. Physical parameterization methods, widely implemented in operational systems like CAMS, calculate u_t from surface physical properties using empirical relationships to achieve global coverage (Rémy et al., 2019, 2022). However, these approaches suffer from limited input data availability and inherent uncertainties in empirical formulations (Klose et al., 2019; Leung et al., 2023). Satellite-based statistical methods offer regional to global coverage but introduce substantial uncertainties through subjective parameter selection and sensitivity to reanalysis datasets. These include dust

https://doi.org/10.5194/essd-2025-628
Preprint. Discussion started: 24 March 2026

optical depth (DOD) based approaches that combine the Moderate Resolution Imaging Spectroradiometer (MODIS; Hsu et al., 2013; Sayer et al., 2013) DOD observations with reanalysis wind data to derive u_t or threshold friction velocity (Draxler et al., 2010; Ginoux and Deroubaix, 2017; Pu et al., 2020), as well as methods using geostationary satellites to track dust emission plumes and relate them to surface wind conditions (AlNasser et al., 2025). Recent comparisons show that different statistical approaches can yield u_t values differing by factors of two in major dust source regions, underscoring the critical need for improved u_t estimation methods at global scales (AlNasser et al., 2025).

Beyond the challenges in determining u_t values, systematic wind speed biases in numerical weather prediction models further degrade dust forecasting accuracy. These biases are substantially amplified through the nonlinear nature of dust emission processes, as even relatively small wind speed deviations can produce substantial differences in predicted dust emissions (Ramon et al., 2019; Faber et al., 2024). Although tuning the emission coefficient in schemes such as those of Marticorena and Bergametti (1995) and Ginoux et al. (2001) can modify the simulated event intensity, it cannot recover emissions lost due to underestimated wind speeds. Therefore, threshold adjustment is essential to maintain consistency between modeled and observed dust activity. Current bias mitigation strategies can be categorized into two main approaches: introducing sub-grid-scale wind variability to represent unresolved turbulent processes (Cakmur et al., 2004; Zhou et al., 2021), and directly adjusting u_t parameters to compensate for systematic wind biases (Heinold et al., 2007). However, many operational systems, such as ECMWF-CAMS, employ u_t values without threshold adjustment to compensate for systematic wind speed underestimation, despite the computational simplicity of the scaling approach (Rémy et al., 2019, 2022; Chen et al., 2025).

To address these fundamental challenges, this study develops a comprehensive solution through the creation of iDust-ut, a high-precision global wind erosion threshold dataset constructed via a multi-source data fusion algorithm. Our approach introduces three key technical innovations: first, establishing reliable station-based u_t reference values by optimizing the agreement between observed and predicted dust emission events from quality-controlled ground observations; second, generating spatially continuous global u_t fields by integrating station constraints with satellite DOD observations and multiple reanalysis wind datasets to minimize single-source uncertainties; third, designing a model-adaptive threshold adjustment scheme that compensates for systematic wind speed biases by maintaining dust emission consistency between models and observations. The resulting dataset undergoes validation against independent field observations and comprehensive evaluation within operational forecasting frameworks, demonstrating substantial improvements in both regional forecast balance and extreme dust event prediction capabilities.

To our knowledge, this is the first global u_t dataset that integrates multi-source observations with model-ready adaptation, offering a practical and scalable solution for improving dust forecasts in operational systems. The remainder of this paper is

https://doi.org/10.5194/essd-2025-628
Preprint. Discussion started: 24 March 2026

organized as follows: Section 2 describes the datasets; Section 3 details the iDust-ut algorithm; Section 4 presents validation against field campaign observations; Section 5 evaluates model application performance; Section 6 discusses strengths and limitations; and Sections 7–9 cover data availability, code access, and conclusions.

2. Datasets

This study employs multiple data sources to develop and validate the iDust-ut global wind erosion threshold dataset (Table 1): ground-based meteorological observations, satellite remote sensing products, numerical model products, and independent validation datasets.

2.1 Ground-Based Meteorological Observations

The Integrated Surface Database (ISD; Smith et al., 2011) is a comprehensive global repository of sub-daily surface weather observations that has been validated for reliability in meteorological model validation and dust emission studies across diverse geographical regions (Xi, 2021; Notaro et al., 2015; Faber et al., 2024; Hao et al., 2024). This study utilizes 10-meter wind speed measurements and present weather phenomenon codes (WW) to develop station-based u_t values. The dust-related WW codes (see Appendix Table A1 for complete definitions) enable identification of dust emission events: observations with WW codes 07, 08, 09, 30–35, and 98 are classified as dust emission events, while WW code 06 represents floating dust.

This study implements a comprehensive quality-control framework through multiple criteria to ensure the reliability of threshold determination: (1) geographic relevance: only stations within one-degree buffer zones of established 1-degree dust source regions (Ginoux et al., 2001) are retained (see Appendix Fig. A1 for station and dust source distribution); (2) statistical adequacy: stations must have at least 10 dust emission events and minimum 500 samples for each calendar month during 2003-2024; (3) data quality: stations with >90 % dust-related weather records, such as specific stations at Northeast Africa, are excluded due to potential data quality concerns; (4) physical realism: stations with >5 % of dust emissions occurring at wind speeds <3.00 m s^{-1} are excluded, as such physically unrealistic events likely indicate weather code or wind speed errors; and (5) wind-dust sensitivity: only stations with Point-Biserial correlation coefficients >0.05 (98 % significance level) between wind speed and dust emission are used, ensuring dust emission responds meaningfully to wind variations (correlation calculation detailed in Appendix D). This multi-criteria approach ensures that threshold determination utilizes only high-confidence observational records.

Hourly PM_{10} measurements from the China National Environmental Monitoring Centre (CNEMC, 2025) are used to evaluate model performance, focusing on Northwestern China stations (70-115° E, 35-50° N) where dust dominates PM_{10} composition, minimizing contamination from other aerosols.

https://doi.org/10.5194/essd-2025-628
Preprint. Discussion started: 24 March 2026

Field campaign u_t measurements from major global dust regions provide direct validation benchmarks for the iDust-ut dataset. These observations encompass North American drylands (Stout and Arimoto, 2010), North Africa (Allen et al., 2013), the Arabian Peninsula (Nelli et al., 2024), and the Taklimakan Desert (Yang et al., 2017), representing diverse surface conditions and climatic regimes typical of global dust source areas. Specific u_t values, site locations, and observation periods are listed in Appendix Table A2.

Table 1. Datasets used in this work.

Data Category	Dataset	Variables	Temporal Coverage	Resolution (Temporal, Spatial lon × lat)	References
Ground Observations	ISD	Present Weather, 10-meter Wind	2003-2024	Sub-daily, Stations	(Smith et al., 2011)
	CNEMC	PM_{10}	2023	Hourly, Station	(CNEMC, 2025)
	Field Campaigns	u_t		Station	(Stout and Arimoto, 2010; Allen et al., 2013; Yang et al., 2017; Nelli et al., 2024)
Satellite Remote Sensing	Terra-MODIS, Aqua-MODIS	AOD, SSA, AE	2003-2024	Daily, 1°×1°	(Platnick, 2015)
	SNPP-VIIRS, NOAA20-VIIRS	AOD, AE	2023	Daily, 1°×1°	(VIIRS Atmosphere Science Team, 2023a, b)
Model Products	ERA5	10-meter wind	2003-2024	Hourly, 0.25°×0.25°	(Hersbach et al., 2020)
	MERRA-2	10-meter wind, DOD, dust concentration, height, pressure	2003-2024	Hourly, 3-hourly, 0.625°×0.5°	(Randles et al., 2017)
	CAMS	10-meter wind, DOD, dust concentration	2023	Hourly, 3-hourly, 0.4°×0.4°	(Rémy et al., 2019, 2022)
	EAC4	DOD, dust concentration	2023	3-hourly, 0.75°×0.75°	(Inness et al., 2019)
Reference Products		u_t based on NCEP/NCAR reanalysis		Monthly, 0.5°×0.5°	(Pu et al., 2020)

https://doi.org/10.5194/essd-2025-628
Preprint. Discussion started: 24 March 2026

2.2 Satellite Remote Sensing Products

Satellite-derived aerosol optical properties provide global-scale spatial coverage essential for extending station-based u_t estimates throughout dust source regions. To maximize temporal coverage and reduce data gaps, this study creates an ensemble-averaged DOD product from multiple satellite observations. MODIS Collection 6.1 products aboard the Terra (MOD08_D3) and Aqua (MYD08_D3) platforms serve as the primary dataset, providing continuous daily 1°×1° gridded aerosol retrievals spanning 2003-2024 (Platnick, 2015); their extended temporal record provides sufficient data for establishing reliable monthly u_t climatology**.** VIIRS observations from SNPP (AERDB_D3_VIIRS_SNPP) and NOAA20 (AERDB_D3_VIIRS_NOAA20) platforms are included in the ensemble for 2023 validation to further reduce missing data (VIIRS Atmosphere Science Team, 2023a, b).

Key parameters from MODIS include daily aerosol optical depth (AOD) at 550 nm, Ångström exponent (AE), and single scattering albedo (SSA) at 470 nm; VIIRS provides AOD and AE but lacks SSA retrievals. To identify dust aerosols, this study adopts the dust identification criteria developed by Pu and Ginoux (2018), which utilize SSA thresholds below 0.99 when available to distinguish mineral dust from highly scattering aerosols. Dust optical depth (DOD) is then derived from AOD using empirical relationships with Ångström exponent values (Anderson et al., 2005) to isolate coarse-mode aerosol contributions (Eq. 1), providing quantitative estimates of dust loading essential for the global u_t algorithm.

$$DOD = AOD \times (0.98 + 0.5089\alpha + 0.0512\alpha^2). \quad (1)$$

2.3 Model Products

2.3.1 Reanalysis Wind Speed Data

High-resolution reanalysis wind fields provide the meteorological foundation linking satellite-observed DOD to surface wind speeds across global dust source regions. To quantify and reduce uncertainties associated with reanalysis product selection, this study derives u_t estimates from two premier reanalysis datasets (ERA5 and MERRA-2) and generates the final product through ensemble averaging**.**

The European Centre for Medium-Range Weather Forecasts Reanalysis version 5 (ERA5; Hersbach et al., 2020) reanalysis provides hourly 10-meter wind speed data at a 0.25° spatial resolution, spanning the period from 2003 to 2024. The Modern-Era Retrospective analysis for Research and Applications version 2 (MERRA-2; Gelaro et al., 2017) from NASA's Goddard Space Flight Center provides complementary hourly 10-meter wind data at a 0.625°×0.5° resolution over the same temporal period. Both products incorporate comprehensive observational data assimilation from surface meteorological stations, radiosondes, and satellite measurements.

https://doi.org/10.5194/essd-2025-628
Preprint. Discussion started: 24 March 2026

Daily maximum wind speeds are utilized in u_t calculations, as dust emission occurs primarily during peak wind conditions. Hourly UTC wind speeds are first converted to local mean solar time before calculating daily maximum, ensuring temporal alignment with satellite observation times (LMST 10:30 for Terra, 13:00 for Aqua, 13:30 for SNPP and NOAA-20; NASA, 2021, 2025a, 2025b).

2.3.2 Other Model Products

Additional model products serve three purposes in this study. For model adaptation, 10-meter wind speed data from ERA5, MERRA-2, and CAMS during 2020–2024 are used to scale the iDust-ut dataset, yielding model-specific u_t values. For performance evaluation, DOD and surface dust concentration from MERRA-2, CAMS, and EAC4 in 2023 are employed to compare model performance, with surface dust concentration converted to PM_{10} for comparison with observational measurements (see Appendix C for conversion methodology). For model initialization, MERRA-2 3D dust concentration, height, and pressure fields from 2023 serve as initial conditions for iDust simulations.

2.4 Reference u_t Datasets

For methodological comparison, the global u_t dataset from Pu et al. (2020), available at https://www.gfdl.noaa.gov/pag-homepage/, is used as a benchmark. This dataset derives u_t values by matching dust event frequencies from MODIS DOD with reanalysis surface wind speed distributions. Pu et al. (2020) tested multiple reanalysis products and found that the NCEP/NCAR reanalysis (Kalnay et al., 1996) produces threshold wind speeds at the lower end of the range. They also examined sensitivity to dust event definitions using two DOD threshold sets: (1) DOD > 0.2 for dust belt regions and DOD > 0.02 for less dusty areas, and (2) DOD > 0.5 for dust belt regions and DOD > 0.05 for less dusty areas, finding that higher DOD thresholds yield higher u_t values (e.g., ~3 m s^{-1} increase in the Sahara). This study uses the NCEP/NCAR reanalysis-based estimates with both DOD threshold configurations for direct comparison, allowing evaluation of improvements from our multi-source data fusion and station-based constraint approach.

3. iDust-ut Algorithm

Accurate global-scale determination of wind erosion thresholds faces significant challenges arising from the sparse distribution of ground observations, substantial spatial heterogeneity of surface properties, and systematic biases in reanalysis wind fields. Traditional approaches suffer from either limited spatial coverage when relying solely on surface measurements (Kurosaki and Mikami, 2007) or single observation source uncertainties when depending exclusively on satellite-based statistical methods (Pu et al., 2020; AlNasser et al., 2025). To address these limitations, this study develops a comprehensive three-stage algorithmic framework that leverages the strengths of multiple observational sources while systematically addressing their individual weaknesses.

https://doi.org/10.5194/essd-2025-628
Preprint. Discussion started: 24 March 2026

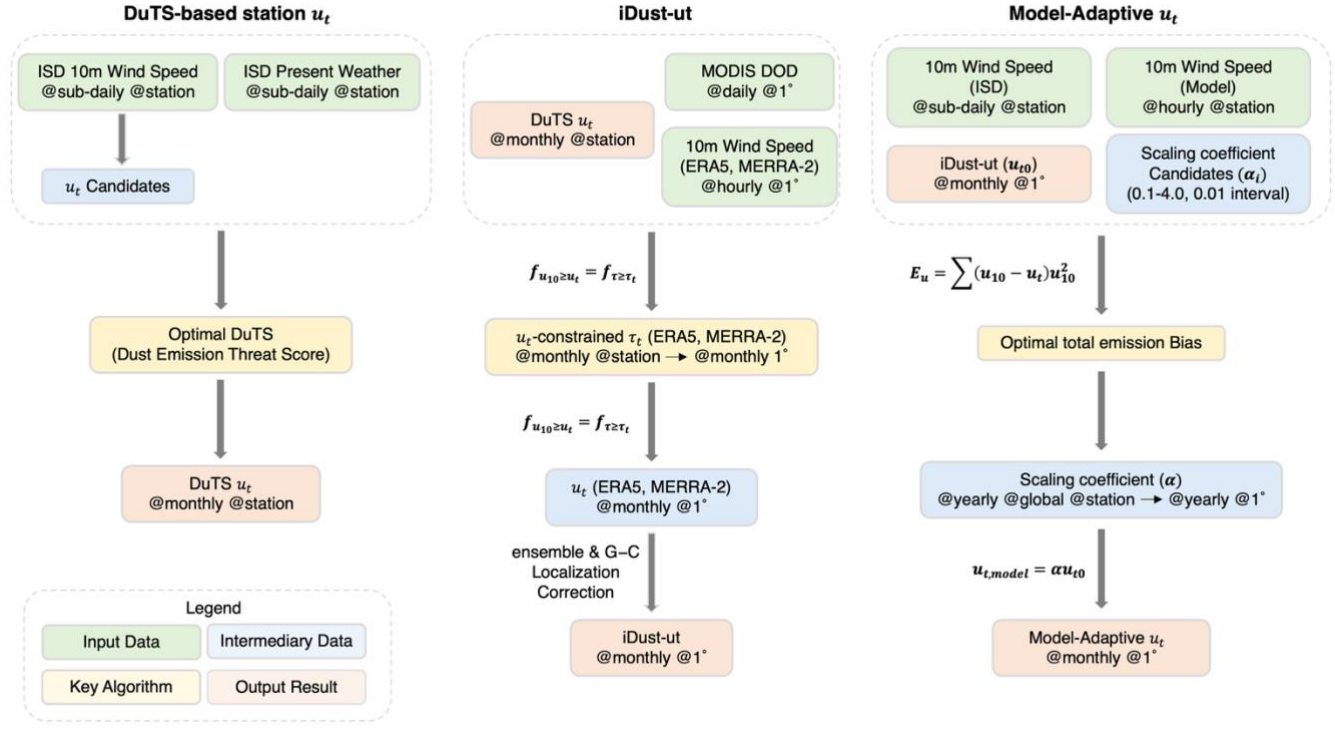

Figure 1. Flow diagram illustrating the development procedure for the global u_t dataset.

3.1 Station u_t Algorithm Based on Optimal Dust Emission Threat Score

Ground-based meteorological observations provide a reliable foundation for determining u_t through direct wind speeds and weather phenomena measurements. Ideally, dust emission would occur only when wind speeds exceed u_t. However, in practice, observed dust emission events (indicated by dust-related weather codes excluding floating dust) and non-emission

https://doi.org/10.5194/essd-2025-628
Preprint. Discussion started: 24 March 2026

events (indicated by floating dust or non-dust weather codes) exhibit considerable overlap in their wind speed distributions, with no clear separation threshold (Fig. 2b).

To address this challenge, the Dust Emission Threat Score (DuTS) is defined as an adaptation of the traditional Threat Score metric in meteorological forecast verification. DuTS quantifies the agreement between observed and threshold-based predicted dust emission events through a contingency table framework (Table 2) and is calculated following Eq. (2):

$$DuTS = \frac{N_{Hit}}{N_{Hit}+N_{FalseAlarm}+N_{MissAlarm}}, \quad (2)$$

where N_{Hit} represents the number of correctly predicted dust emission events (observed emission with wind speed exceeding the threshold), $N_{FalseAlarm}$ denotes the number of false alarms (no observed emission despite wind speed exceeding the threshold), and $N_{MissAlarm}$ indicates the number of missed events (observed emission with wind speed below the threshold). The DuTS ranges from 0 to 1, with higher values indicating better agreement between threshold-based predictions and observations. A DuTS of 1 represents perfect prediction, while a value of 0 indicates no skill.

Table 2. Contingency table for dust emission prediction based on wind speed versus observation.

Dust Emission	Predicted Yes ($u_{10} > u_t$)	Predicted No ($u_{10} \leq u_t$)
Observed Yes	Hit	Miss Alarm
Observed No	False Alarm	True Negative

The DuTS-based threshold determination algorithm is applied to station-level sub-daily wind speed and weather phenomenon records that are aggregated into calendar-month sample pools across years (e.g., all March data from 2003-2024). This monthly climatological approach accounts for seasonal variations in dust emission dynamics while maintaining sufficient sample sizes for robust statistical analysis. The algorithm comprises four steps:

(1) Data quality control and preprocessing: Two categories of samples are excluded to ensure physical consistency. First, all precipitation events (WW codes 50-97 and 99) are removed, as precipitation suppresses dust emission regardless of wind speed. Second, dust emission records at wind speeds below 3 m s^{-1} are filtered out, as these are likely to represent observational errors or misclassified weather phenomena.

(2) u_t candidate generation: Within each monthly sample pool, all sub-daily observations are sorted by wind speed in ascending order, with their corresponding dust emission status recorded. At each transition from non-emission to emission conditions, a threshold candidate is identified as the midpoint between the two consecutive wind speeds (illustrated by upward triangles in Fig. 2a). Candidates are retained only when the wind speed difference at the transition does not exceed

https://doi.org/10.5194/essd-2025-628
Preprint. Discussion started: 24 March 2026

1.00 m s^{-1}, indicating adequate observational resolution for reliable threshold identification. This procedure typically generates multiple threshold candidates per monthly sample pool.

(3) DuTS calculation and optimization: For each threshold candidate ($u_{t,candidate,i}$), the DuTS is calculated using Eq. (2) by applying it to the entire monthly sample pool as follows: each observation in the sample pool is classified as a predicted emission event if $u_{10} > u_{t,candidate,i}$, or as a predicted non-emission event if $u_{10} \leq u_{t,candidate,i}$. These predictions are then compared against the actual observed dust emission status to determine N_{Hit}, $N_{FalseAlarm}$, and $N_{\mathrm{MissAlarm}}$, from which the DuTS is calculated. Lower threshold candidates tend to generate more false alarms while higher threshold candidates tend to produce more miss alarms. The candidate yielding the maximum DuTS represents the optimal threshold that best balances these two types of errors. To reduce statistical noise from individual candidates, all candidates within 0.02 of the maximum DuTS (indicated by red triangles in Fig. 2c) are combined through DuTS-weighted averaging following Eq. (3):

$$u_t = \frac{\Sigma(DuTS_i \times u_{t,candinate,i})}{\Sigma DuTS_i} \quad (3)$$

where the summation includes only candidates satisfying $DuTS_i \geq DuTS_{max} - 0.02$.

(4) Final Quality control: Two criteria ensure reliable threshold determination for each monthly sample pool. First, stations with maximum DuTS below 0.10 are excluded, indicating insufficient predictive skill. Second, stations where the maximum DuTS improves by less than 0.05 compared to the baseline DuTS are rejected. The baseline DuTS is calculated by treating the minimum u_t candinate in the monthly sample pool as the threshold; this baseline typically yields high false alarm rates and serves as a reference for assessing meaningful improvement.

Tazhong Station Example: Figure 2b-c demonstrates the algorithm applied to Tazhong station (83.667° E, 39.0° N) using May observations from 2003 to 2024. Dust emission events (red markers) predominantly occur above 5.00 m s^{-1}, while non-dust conditions (blue markers) span the entire wind speed range (Fig. 2b). Through traversal of threshold candidates, the algorithm identifies a maximum DuTS value of 0.59 at approximately 6.0 m s^{-1} (Fig. 2c). However, rather than selecting this single candidate, the final threshold is determined by weighted averaging of multiple high-performing candidates to enhance robustness. Specifically, all candidates with $DuTS \geq 0.57$ (i.e., $DuTS_{max} - 0.02$, indicated by the horizontal gray dashed line) are ensemble-averaged using DuTS-weighted averaging (Eq. 3). These selected candidates (red triangles) span a range of approximately 5–6 m s^{-1}, and their weighted average yields the final threshold of $u_t = 5.22$ m s^{-1} (vertical black dashed line in Fig. 2c).

https://doi.org/10.5194/essd-2025-628
Preprint. Discussion started: 24 March 2026

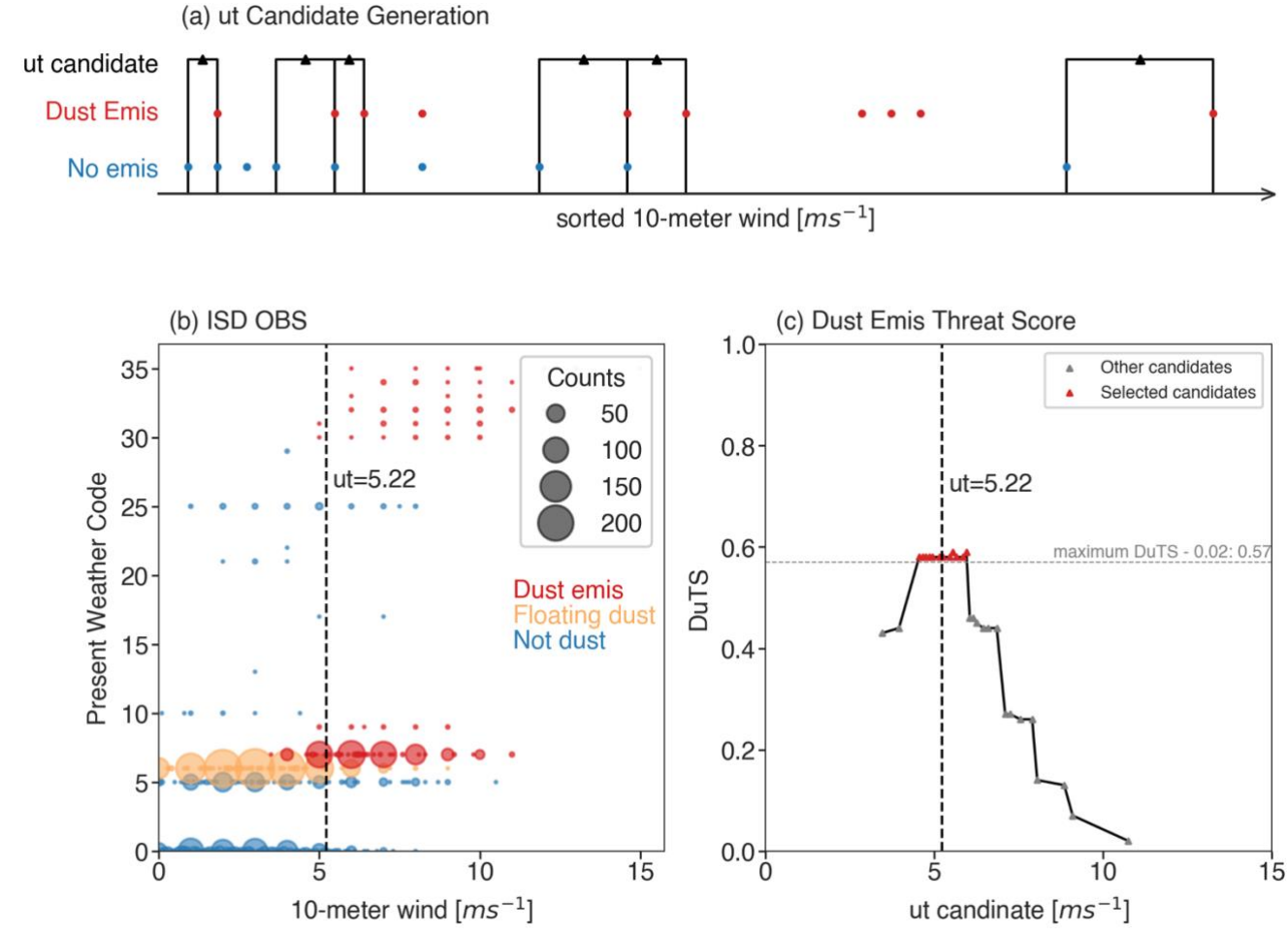

Figure 2. Illustration of the DuTS-based threshold determination algorithm applied to Tazhong station (83.667° E, 39.0° N) using May data (2003-2024). (a) Schematic illustration of threshold candidate generation: blue and red points represent non-emission and dust emission events respectively, with upward triangles indicating candidates defined as midpoint between two consecutive wind speed observations where dust emission status transitions from non-emission to emission. (b) Distribution of 10-meter wind speed versus weather codes: blue, orange, and red points represent non-dust weather, floating dust, and dust emission events, respectively. Marker size is proportional to the count of occurrences. (c) Dust Emission Threat Score (DuTS) as a function of threshold candidates: red triangles indicate candidates above the horizontal gray dashed line ($DuTS_i \geq DuTS_{max} - 0.02$), which are selected for weighted averaging to determine the final u_t; gray triangles represent other candidates. The vertical black dashed line marks the final threshold (5.22 m s^{-1}).

3.2 Station-constrained Global u_t Algorithm

3.2.1 Algorithm Overview

Direct interpolation of station-derived u_t values to generate global gridded thresholds introduces substantial uncertainties. Wind erosion thresholds vary significantly with soil texture and vegetation coverage, and topographic barriers create sharp

https://doi.org/10.5194/essd-2025-628
Preprint. Discussion started: 24 March 2026

spatial discontinuities in surface characteristics. These complex patterns cannot be captured by sparse meteorological stations, rendering direct interpolation inadequate for mapping global threshold.

To address these limitations, this study adopts and enhances the indirect approach proposed by Pu et al. (2020). This method leverages satellite dust optical depth (DOD, τ) observations combined with reanalysis wind fields, both of which are gridded global datasets well-suited for global-scale applications. The approach matches dust emission frequencies calculated from two independent sources: reanalysis wind speeds with wind erosion thresholds, and satellite DOD observations with a DOD threshold (τ_t). This relationship is expressed as:

$$f_{u_{10}>u_t} = f_{\tau>\tau_t}, \quad (4)$$

where both frequencies are calculated for each month using data from 2003 to 2024.

Pu et al. (2020) developed this frequency-matching approach using predefined τ_t values (0.2 for dust belt regions, 0.02 for less dusty areas) applied uniformly across broad geographical regions. While their method demonstrated global applicability, the selection of τ_t values was empirical. This study improves upon their methodology through a station-based constraint system: the DOD threshold (τ_t) is derived at each station location by inverting Eq. (4) using the high-quality monthly station u_t values from Sect. 3.1, rather than being predefined. The gridded τ_t field is then generated by interpolating these station-constrained τ_t values, ensuring that the final gridded u_t remains consistent with station-derived thresholds while leveraging the global spatial coverage of satellite data. This data-driven approach eliminates the need for arbitrary parameter selection and regional divisions.

Given that reanalysis wind fields contain inherent dataset-specific biases, this study applies the algorithm to two independent reanalysis products (ERA5 and MERRA-2) to assess and minimize threshold uncertainties arising from reanalysis selection**.** For each reanalysis, the station-constraint mechanism adapts τ_t to its wind characteristics, allowing independent derivation of global u_t fields that reproduce station-derived thresholds.

3.2.2 Global u_t Generation with Station Constraints

For each reanalysis dataset (ERA5 and MERRA-2), global gridded thresholds are generated through the following five-step procedure: station u_t values constrain τ_t interpolation, followed by frequency matching to derive global u_t fields.

(1) Station τ_t calculation: Monthly τ_t values at each station are calculated using Eq. (4), combining station thresholds from Sect. 3.1 with reanalysis wind speeds and satellite DOD interpolated to station locations. This step translates the station threshold into the satellite DOD space, where τ_t adapts to the wind characteristics of each reanalysis dataset, ensuring that the subsequently derived u_t matches the station-based value.

https://doi.org/10.5194/essd-2025-628
Preprint. Discussion started: 24 March 2026

(2) τ_t spatial interpolation: Station τ_t values are interpolated to a global grid using inverse distance cubed weighting. For each grid point, interpolation uses all stations within a 2000 km radius, but only when at least three valid stations are available; otherwise, no value is assigned. To ensure robust interpolation, station τ_t values exceeding 1.5 standard deviations from the overall mean are excluded as outliers, and multiple stations within the same grid cell are pre-averaged to prevent overweighting of dense station clusters.

(3) τ_t gap filling and smoothing: Monthly gaps in data-sparse regions are filled using annual mean τ_t values. The gap-filled field then undergoes three iterations of 81-point spatial smoothing to remove small-scale variability and ensure spatial continuity.

(4) τ_t local correction: To preserve local accuracy near stations, the Gaspari-Cohn localization method (Gaspari and Cohn, 1999) is applied to adjust the smoothed τ_t field. The final τ_t combines the smoothed field with weighted corrections from nearby stations:

$$\tau_t(i,j) = \tau_{t,smoothed}(i,j) + \Delta\tau_t(i,j), \quad (5)$$

where $\Delta\tau_t(i,j)$ is the smoothed local correction obtained by applying 9-point smoothing to the raw correction field calculated following Eq. (6):

$$\Delta\tau_t(i,j) = \frac{\Sigma_s R^{GC}\left(\frac{d_s}{R_{loc}}\right)\frac{1}{d_s+\varepsilon}\Delta\tau_{t,s}}{\Sigma_s \frac{1}{d_s+\varepsilon}}, \quad (6)$$

where $\Delta\tau_{t,s}$ is the difference between τ_t at station s and the smoothed τ_t at station location; R^{GC} is the Gaspari-Cohn localization function (see Appendix B for details); d_s is the distance from the grid point to station s; $\varepsilon = 1e^{-5}$ km is used to prevent division by zero; and R_{loc} is the localization radius set to 300 km. This smaller radius prevents excessive influence from desert margin values on interior desert regions, such as areas near the Rub' al Khali Desert.

(5) Global threshold derivation: At each grid point, wind erosion thresholds are determined from the final τ_t field using Eq. (4), with the threshold value derived to satisfy the frequency matching criterion between reanalysis winds and the merged MODIS DOD. Missing DOD values and their temporally/spatially corresponding wind speeds are excluded from the frequency matching to ensure consistent data pairing.

3.2.3 Reanalysis-based τ_t and u_t Comparison

Figure 3 illustrates the station-constrained DOD threshold (τ_t) and resulting wind erosion thresholds (u_t) derived from ERA5 and MERRA-2 surface wind fields. Although the spatial patterns of τ_t show similar geographical distributions

https://doi.org/10.5194/essd-2025-628
Preprint. Discussion started: 24 March 2026

between the two reanalysis datasets (Fig. 3a and 3b), with elevated values concentrated in major dust source regions, substantial magnitude differences exist. ERA5-derived τ_t values are systematically higher than those from MERRA-2, particularly evident in the Sahara, where ERA5 reaches 0.6-0.8 while MERRA-2 remains at 0.4-0.6. The seasonal cycles (Fig. 3c and 3d) further highlight these magnitude differences: Northern Hemisphere τ_t from ERA5 peaks at 0.5-0.6 during April-August, approximately 20-30 % higher than the 0.4-0.5 values from MERRA-2. These substantial τ_t differences reflect the inherent wind speed characteristics of each reanalysis dataset.

Despite the pronounced differences in τ_t values, the derived u_t fields (Fig. 3e-f) demonstrate remarkable consistency between ERA5 and MERRA-2. Both datasets capture identical spatial features with higher thresholds in South Africa, Australia, and the Gobi Desert, and lower values in the Taklimakan Desert and the Arabian Peninsula. The seasonal cycles (Fig. 3g-h) reveal that the two reanalysis-derived thresholds closely track each other in the dust belt region, with differences typically below 1 m s^{-1}. This convergence in u_t despite 20-30 % differences in τ_t demonstrates the effectiveness of the adaptive τ_t approach: the weaker wind speeds in ERA5 require higher τ_t values, whereas the stronger winds in MERRA-2 require lower τ_t values, yet both yield similar u_t estimates through the frequency-matching framework. By allowing τ_t to adapt to each reanalysis wind fields while maintaining consistency with station u_t values, this station-constrained approach effectively decouples the final u_t estimates from reanalysis-specific wind biases, representing a fundamental advancement over the fixed τ_t approach of Pu et al. (2020).

3.2.4 Uncertainty Quantification and iDust-ut Ensemble

To quantify the uncertainty arising from reanalysis selection and generate the final iDust-ut product, this section first assesses the differences between thresholds derived from ERA5 and MERRA-2, then combines them through ensemble averaging. Reanalysis-dependent uncertainty is quantified following Eq. (7):

$$u_{t,uncert} = \frac{1}{12} \Sigma_{month} \left| u_{t,ERA5} - u_{t,MERRA-2} \right|. \quad (7)$$

Figure 4a shows the spatial distribution of reanalysis-dependent uncertainty. The two datasets demonstrate high consistency, with uncertainties of less than 1 m s^{-1} across most regions. South America exhibits the highest uncertainties, followed by North America. These results demonstrate the effectiveness of station constraints in minimizing reanalysis-dependent uncertainties.

The final iDust-ut dataset is generated by averaging the ERA5 and MERRA-2 thresholds, followed by a local correction using DuTS station observations. The correction applies the Gaspari-Cohn localization method described in Sect. 3.2.2, but uses direct station-gridded u_t differences rather than τ_t differences. To focus on active dust source regions, the dataset is then masked to dust source regions using the 1° dust source function from Ginoux et al. (2001), with remaining gaps filled

https://doi.org/10.5194/essd-2025-628
Preprint. Discussion started: 24 March 2026

through nearest-neighbor interpolation to ensure complete coverage within the masked domain. Outside the masked domain, a 2-degree nearest-neighbor buffer is applied beyond the dust source boundary, followed by a 5-degree linear transition to a global default value of 6.5 m s^{-1}, ensuring full global coverage for model applications. Note that all figures presented in this study are based on the masked domain only.

Figure 4b presents the annual mean iDust-ut (shaded). The iDust-ut shows clear regional patterns: the Taklimakan Desert exhibits the lowest thresholds, followed by relatively low values across the Arabian Peninsula and North Africa. In contrast, the Gobi Desert and regions with less frequent dust activity (North America, South America, South Africa, and Australia) show notably higher thresholds.

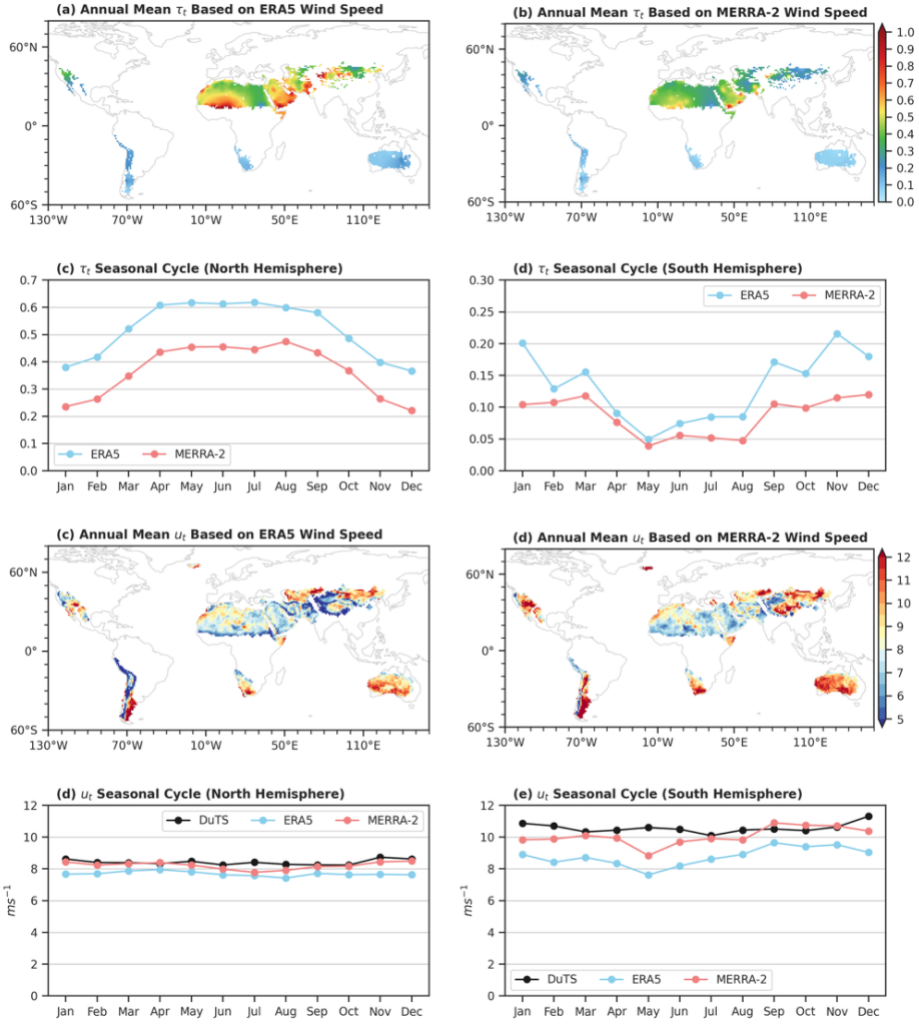

Figure 3. Station-constrained DOD thresholds (τ_t) and wind erosion thresholds (u_t) derived from ERA5 and MERRA-2 wind speed. (a-b) Annual mean τ_t fields derived from ERA5 and MERRA-2, respectively. (c-d) Monthly mean τ_t seasonal cycles for Northern and Southern Hemispheres. (e-f) Annual mean u_t derived from ERA5 and MERRA-2. (g-h) Monthly mean u_t seasonal

https://doi.org/10.5194/essd-2025-628
Preprint. Discussion started: 24 March 2026

390 **cycles for Northern and Southern Hemispheres comparing ERA5 (blue), MERRA-2 (red), and DuTS-derived station values (black).**

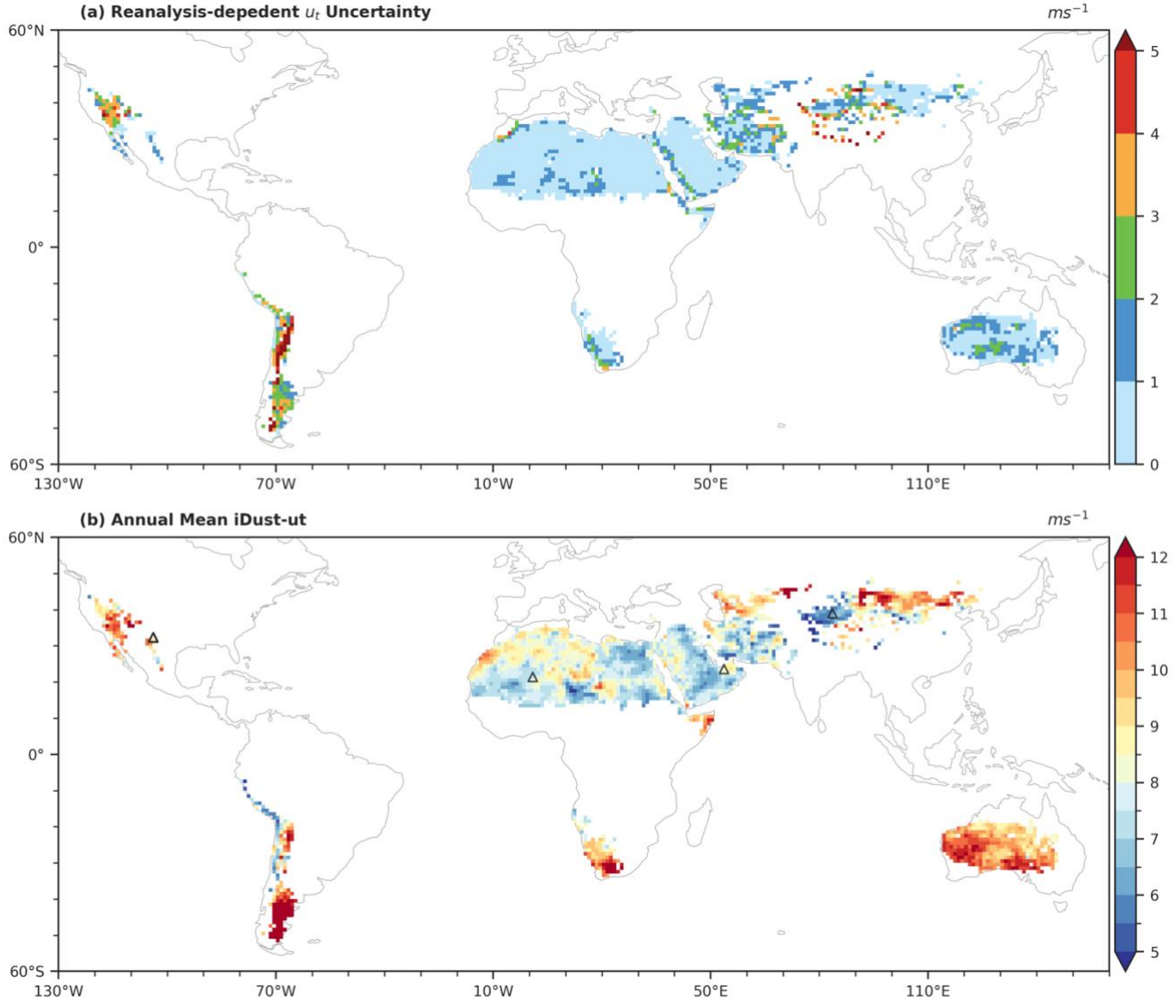

Figure 4. Spatial distribution of (a) reanalysis-dependent u_t uncertainty and (b) annual mean iDust-ut. Black triangles in panel (b) indicate locations of field campaign stations used for independent validation.

395 **3.3 Model-Adaptive u_t Algorithm based on Total Emission Consistency**

Although the iDust-ut dataset provides observation-based objective thresholds, direct implementation in operational dust forecast models may introduce errors due to systematic wind speed biases in numerical weather prediction systems. To

https://doi.org/10.5194/essd-2025-628
Preprint. Discussion started: 24 March 2026

mitigate this issue, this study proposes a linear scaling approach to adapt thresholds to individual model wind characteristics. The model-adaptive threshold ($u_{t,model}$) is obtained through linear scaling:

$$u_{t,model} = \alpha\, u_{t0}, \tag{8}$$

where u_{t0} is the iDust-ut and α is the scaling coefficient. The optimal scaling coefficient (α) is determined by minimizing the difference between emission proxies calculated from model winds and those calculated from observed winds:

$$\Delta E_u(\alpha_i) = \mid E_{u,model} - E_{u,OBS} \mid = \mid E_u(u_{10,model}, \alpha_i u_{t0}) - E_u(u_{10,ISD}, u_{t0}) \mid \tag{9}$$

where E_u represents the monthly accumulated wind-driven emission proxy calculated as:

$$E_u(u_{10}, u_t) = \sum u_{10}^2 (u_{10} - u_t). \tag{10}$$

The calculation of model-adaptive u_t follows these steps:

(1) E_u calculation: At each station, emission proxies are calculated using Eq. (10) for both ISD observed winds with iDust-ut and model winds (bilinearly interpolated to station locations) with candidate scaled thresholds ($u_{t,\text{model}} = \alpha_i u_{t0}$).

(2) Station-specific α optimization and quality control: For each station, the optimal scaling coefficient α is determined by minimizing $\Delta E_u(\alpha_i)$ (Eq. 9) through iterative search over α ∈ [0.01, 4] with 0.01 increments. Quality control criteria are applied to ensure α reliability. Station-derived α values are retained only if they meet the following criteria: total wind speed samples ≥ 100; wind speed correlation between ISD observations and model ≥ 0.40 with p-value ≤ 0.02; at least 5 emission events in ISD observations ($u_{10,\text{ISD}} > u_{t0}$) and at least 5 emission events in model simulations ($u_{10,\text{model}} > \alpha u_{t0}$). These criteria ensure scaling factors are based on sufficient statistical samples and are physically reasonable.

(3) Global background scaling coefficient: Recognizing that station coverage is sparse in many dust source regions, a globally uniform scaling coefficient (α_{global}) is determined as the background field for the entire domain. This α_{global} minimizes the mean difference between model-based and observation-based emission proxies all available stations and samples, capturing the model's domain-scale systematic wind speed bias.

(4) Local correction and smoothing: Annual α values at quality-controlled stations are used for local correction, with outliers beyond 2 standard deviations excluded. The Gaspari-Cohn localization method is employed with a 600 km radius, applying corrections only when more than 3 stations are available within the $2R_{loc}$ range. A single 81-point filter smooths the corrected field.

(5) Model-adaptive u_t generation: The final model-adaptive u_t is obtained by multiplying the iDust-ut by the scaling factors:

https://doi.org/10.5194/essd-2025-628
Preprint. Discussion started: 24 March 2026

Open Access Earth System Science Data Discussions

$$u_{t,model}(i,j) = \alpha(i,j)u_{t0}(i,j). \quad (11)$$

where i and j represent grid indices in longitude and latitude, respectively.

Figures 5a-d compare monthly model-derived and ISD-derived E_u at each station for 2023. All models exhibit substantial underestimation relative to ISD-derived E_u with numerous missed emission events, highlighting the necessity of u_t adaptation. iDust demonstrates the best performance across all metrics (correlation, MAE, and mean bias), likely attributable to its high spatial resolution that enables superior extreme wind simulation.

Figure 5e displays global scaling factors for various models from 2020 to 2024, with scatter points representing results from individual years and horizontal lines representing results calculated using all samples from 2020-2024 combined. iDust exhibits the most favorable scaling factor with a global average of 0.96, confirming excellent high wind speed simulation accuracy. MERRA-2 exhibits a scaling factor of approximately 0.83, indicating moderate underestimation of high wind speeds. In contrast, ERA5 and CAMS exhibit more pronounced systematic underestimation, with scaling factors of approximately 0.64 and 0.60, respectively. All datasets maintain good temporal stability with minimal interannual variability, demonstrating the robustness of the global scaling approach. Spatially, the iDust scaling coefficients (Fig. 5f) exhibit considerable heterogeneity. The Gobi and Taklimakan deserts show overestimation (α > 1), whereas the Sahara Desert and Arabian Peninsula exhibit predominantly underestimation.

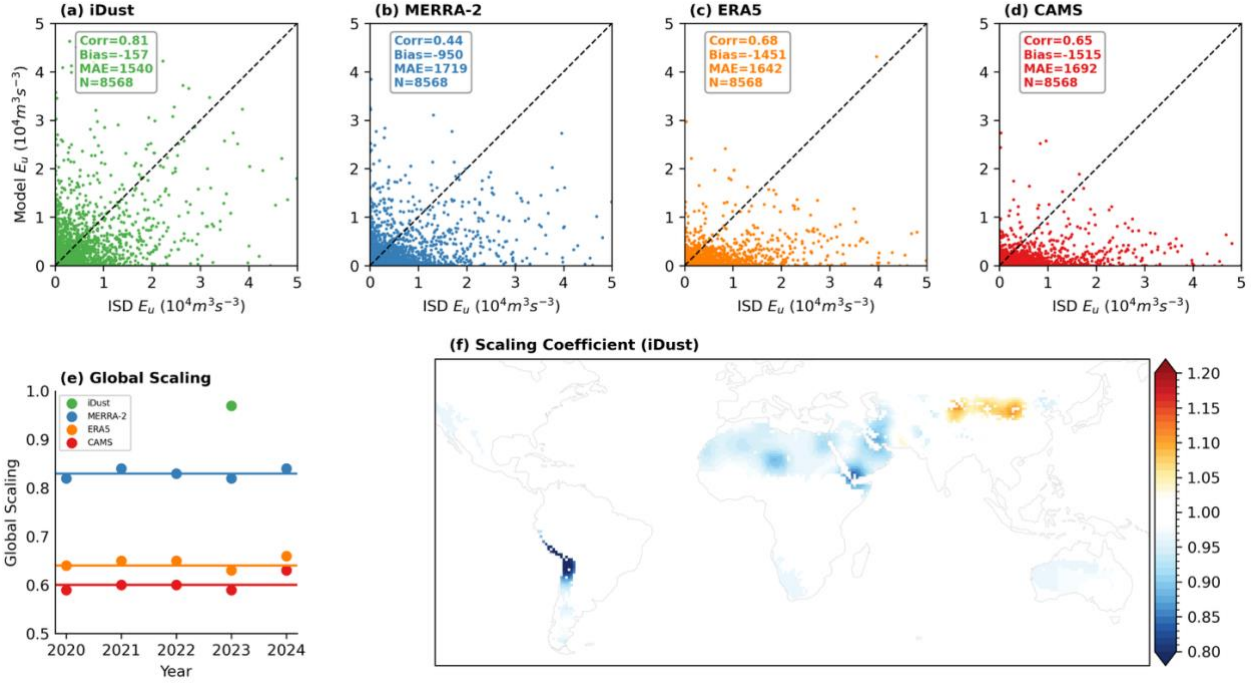

https://doi.org/10.5194/essd-2025-628
Preprint. Discussion started: 24 March 2026

Open Access Earth System Science Data Discussions

Figure 5. Evaluation of dust emission consistency and scaling coefficients for u_t adjustment. (a-d) Comparison between model-derived E_u and ISD-derived E_u without u_t adjustment for different dust models in 2023: (a) iDust, (b) MERRA-2, (c) ERA5, and (d) CAMS. Scatter points represent monthly values at individual stations, with statistical metrics shown in each panel. The black dashed line indicates the 1:1 reference line. (e) Global scaling coefficients derived for each year from 2020-2024, with horizontal lines representing the overall global scaling coefficient calculated using all samples from 2020-2024. (f) Spatial distribution of gridded iDust scaling coefficients derived from 2023 wind speed data.

4. iDust-ut Dataset Validation

To validate the accuracy of the iDust-ut dataset, this study evaluated its performance against five independent u_t observations from major global dust source regions, with station locations indicated by the black triangles in Figure 4b (details in Appendix Table A2). These observational data cover dust-active regions, including North American arid areas (Stout and Arimoto, 2010), the North African Sahel region (Allen et al., 2013), the Arabian Peninsula (Nelli et al., 2024), and the Taklimakan Desert (Yang et al., 2017).

The validation results (Fig. 6) demonstrate strong agreement between the iDust-ut dataset and field observations, achieving a correlation coefficient of 0.93 (significant at 95 % confidence level) and a mean absolute error of 0.80 m s^{-1}. iDust-ut substantially outperforms the NCEP/NCAR-based estimates from Pu et al. (2020) (Fig. 6b and c), which show weaker correlations and larger biases at the same validation sites. The superior accuracy of iDust-ut is primarily attributable to methodological advances: the multi-source data fusion leverages global coverage from DOD observation and reanalysis winds, while station-based DuTS optimization establishes reliable threshold constraints from observed dust emission events at meteorological stations. Additional factors, including differences in study period (2003-2024 vs. 2003-2015) and reanalysis products (ERA5/MERRA-2 vs. NCEP/NCAR), may also contribute to the performance differences.

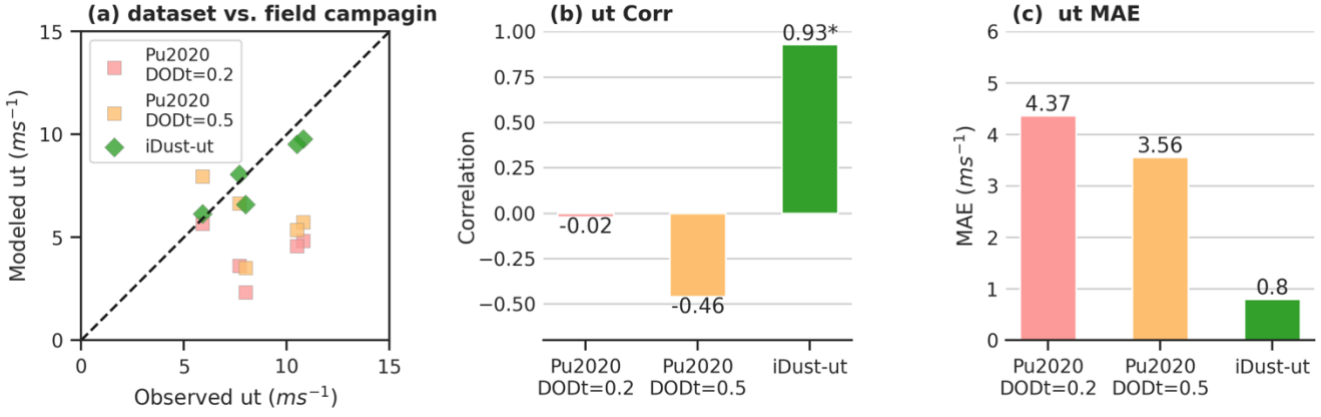

Figure 6. (a) Validation scatter plot comparing gridded u_t dataset with field-observed u_t, where green diamonds represent this study's iDust-ut, pink and orange squares represent results from Pu et al. (2020) method under $DOD_t = 0.2$ and $DOD_t = 0.5$ conditions respectively, and the black dashed line shows the 1:1 reference line; bar charts comparing (b) correlation coefficients

https://doi.org/10.5194/essd-2025-628
Preprint. Discussion started: 24 March 2026

and (c) mean absolute error (MAE) of u_t estimation results from different methods. * in panel (c) indicate statistical significance at the 95 % confidence level.

5. Model Implementation and Performance Evaluation

5.1 Numerical Model Framework

The iDust model serves as the evaluation framework for assessing the iDust-ut dataset performance in operational dust forecasting applications. iDust is an advanced global dust-weather integrated forecasting system that couples dust emission, transport, and deposition processes directly within the dynamical core of numerical weather prediction models (Chen et al., 2025). This direct integration enables computationally efficient dust simulations, facilitating timely high-resolution dust calculations for operational forecasting. The model configuration employs a 12.5 km horizontal resolution with MERRA-2 three-dimensional dust concentration fields serving as the initial conditions for the forecast experiments.

Similar to the GOCART dust emission scheme (Ginoux et al., 2001), dust emission in iDust is parameterized using a cubic wind speed formulation following Eq. (12):

$$F_p = C\,S\,S_p u_{10}^3 \left[1 - \left(\frac{u_t}{u_{10}}\right)^{n_t}\right], \quad if\ u_{10} > u_t, \tag{12}$$

where F_p is the surface upward dust flux for particle size class p (unit: μg m^{-2} s^{-1}), C is a dimensional coefficient (unit: μg s^2 m^{-5}), S is the 1 degree topography-based dust source function (Ginoux et al., 2001), S_p is the mass fraction for each size class with five size bins (radius of 0.1-1, 1-2, 2-3, 3-6, and 6-10 μm) corresponding to mass fractions of [0.05, 0.15, 0.3, 0.27, 0.23], u_{10} is the 10-meter horizontal wind speed, u_t is the wind erosion threshold, and $n_t = 1$ is an exponential parameter introduced by Chen et al. (2025) to fine tune dust emission responses to surface wind. Dust emission occurs only when $u_{10} > u_t$.

5.2 Simulation Design

To evaluate the effects of the u_t dataset on dust simulation accuracy, three experiments are designed based on the iDust model (Table 3). The CTRL experiment uses a globally uniform u_t=6 m s^{-1} as the baseline configuration. The iDust_ut experiment applies the iDust-ut dataset. The iDust_ut_adpt experiment adopts the iDust-ut dataset with adaptive adjustment. The dust emission coefficient C in Eq. (12) is adjusted across experiments to maintain overall emission consistency with observations, compensating for the impact of u_t changes on total emission.

All experiments use a horizontal resolution of 12.5 km with 63 vertical levels extending from the surface to a model top at 64.247 Pa, and are initialized with MERRA-2 three-dimensional dust concentration fields and GFS meteorological fields. The simulations span the entire year of 2023 to capture dust activity across all seasons. Using a cycling forecast approach,

https://doi.org/10.5194/essd-2025-628
Preprint. Discussion started: 24 March 2026

five-day forecasts are initialized every five days at 00 UTC throughout 2023. For comparative evaluation, iDust results are also compared with mainstream dust products, including ECMWF-CAMS forecasts (Rémy et al., 2019, 2022), NASA MERRA-2 (Randles et al., 2017), and CAMS EAC4 reanalysis (Inness et al., 2019).

Table 3. iDust model simulation configurations

Simulation	u_t	C parameter ($\mu g\ s^2\ m^{-5}$)
CTRL	6 m s^{-1} (constant)	0.4
iDust_ut	iDust-ut dataset	0.9
iDust_ut_adpt	Adaptive adjusted iDust-ut dataset	1.0

5.3 Validation Strategy

The validation framework evaluates model performance at two levels: (1) surface PM_{10} validation using ground stations in Northwest China (70-115° E, 35-50° N), and (2) satellite DOD validation covering the dust belt region (30° W-110° E, 0°-50° N). Ground validation uses hourly PM_{10} observations from the China National Environmental Monitoring Centre (CNEMC), while satellite validation employs merged MODIS and VIIRS DOD data.

Model performance is evaluated using multiple statistical metrics: Pearson correlation coefficients for temporal consistency, mean absolute error (MAE) for simulation bias, and Threat Scores for dust event capture capability (see Appendix D for calculation details). For all metrics, temporal statistics are first computed at each individual station or grid point, then spatially averaged across all locations. For DOD validation, all metrics are weighted by the cosine of latitude.

5.4 Validation Results

5.4.1 PM_{10} Forecasting Enhancement by the iDust-ut Dataset

Figure 7 presents a comprehensive evaluation of daily mean PM_{10} simulation performance for different dust models in Northwest China. Panels a-f show the spatial distribution of PM_{10} biases for each model, while panels g-j compare statistical performance metrics including correlation coefficients, mean absolute error (MAE), and Threat Scores (TS) at different intensity thresholds.

https://doi.org/10.5194/essd-2025-628
Preprint. Discussion started: 24 March 2026

The spatial distribution of PM_{10} biases exhibit substantial regional variation (Fig. 7a-f). The iDust_CTRL configuration shows a significant spatial imbalance, with positive biases in the eastern Gobi Desert contrasting with negative biases in the western Taklimakan Desert. Both iDust_ut and iDust_ut_adpt substantially improve these patterns, achieving more uniform spatial distributions with reduced bias magnitudes across the domain. Among comparison models, CAMS forecasts display systematic negative biases throughout Northwest China. EAC4 reanalysis exhibits mixed patterns with negative biases in the Taklimakan Desert and positive biases in the Gobi Desert, whereas MERRA-2 demonstrates positive biases in northern Xinjiang. iDust-ut effectively resolves the regional emission imbalance in the control simulation.

Temporal correlation analysis reveals significant differences among models in capturing PM_{10} variation patterns (Fig. 7g). Implementation of the iDust-ut dataset yields substantial improvements in temporal prediction capability, with iDust_ut_adpt achieving the highest correlation coefficient of 0.55 and iDust_ut reaching 0.54, both representing notable enhancements over the control configuration at 0.48. These optimized configurations outperform established reanalysis products with satellite data assimilation, including EAC4 at 0.42 and MERRA-2 at 0.43. CAMS exhibits the poorest temporal correlation at 0.27, indicating fundamental limitations in its dust process representation for this region.

The mean absolute error analysis shows overall prediction accuracy (Fig. 7h). MERRA-2 achieves the lowest MAE at 70.19 μg m^{-3}, demonstrating superior performance in this metric. The optimized iDust configurations follow closely, with iDust_ut_adpt recording 72.39 μg m^{-3} and iDust_ut showing 74.94 μg m^{-3}, representing approximately a 10 % reduction in MAE compared to the control configuration. EAC4 and CAMS exhibit higher MAE values of 82.71 and 78.11μg m^{-3}, respectively. These improvements demonstrate the effectiveness of the iDust-ut dataset in reducing systematic errors.

The Threat Score analysis reveals substantial differences in forecasting capabilities for dust events of varying intensities. For moderate-intensity events with PM_{10} concentrations between 300 and 1000 μg m^{-3}, the optimized iDust models demonstrate distinct advantages. The iDust_ut_adpt configuration achieves the highest Threat Score of 17.61 %, followed by iDust_ut at 16.06 %, both exceeding the control simulation at 12.34 % and substantially outperforming CAMS at 2.38 %. EAC4 performs competitively at 15.35 %, while MERRA-2 achieves 11.64 %. For extreme dust events exceeding 1000 μg m^{-3}, performance disparities become more pronounced. The iDust_ut_adpt configuration maintains the strongest performance with a Threat Score of 36.25 %, while iDust_ut achieves 31.51 %, approximately doubling the control configuration at 17.39 %. EAC4 shows reasonable performance at 26.94 %, while the MERRA-2 Threat Score decreases to 2.24 %. CAMS completely fails to capture extreme events, registering a Threat Score of 0.00 %.

In summary, incorporating the iDust-ut dataset achieves substantial PM_{10} simulation improvements in Northwest China across all evaluation metrics. The optimized iDust configurations effectively resolve the spatial bias imbalance between the Gobi Desert and Taklimakan Desert present in the control simulation, achieving superior temporal correlation coefficients

https://doi.org/10.5194/essd-2025-628
Preprint. Discussion started: 24 March 2026

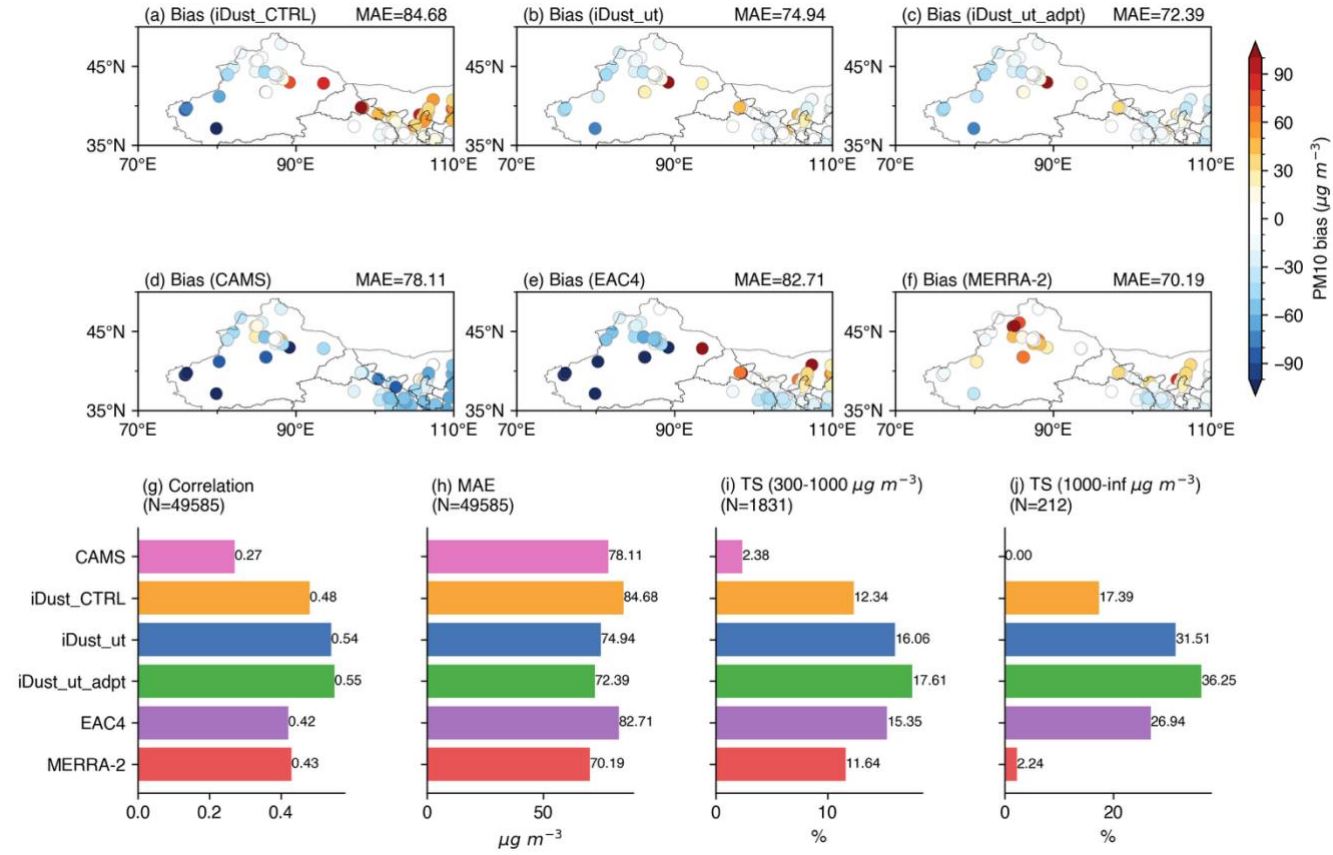

Figure 7. Daily mean PM_{10} simulation evaluation of different dust models in Northwest China (70-115° E, 35-50° N). (a-f) Spatial distribution of PM_{10} biases and PM_{10} simulation performance statistics for different models, including (g) correlation coefficients, (h) mean absolute error (MAE), and (i-j) Threat Scores (TS) under different thresholds (in the range of 300-1000 μg m^{-3} and PM_{10} > 1000 μg m^{-3}).

5.4.2 DOD Forecasting Enhancement by the iDust-ut Dataset

DOD simulation evaluation provides key insights into model performance across the broader dust belt region. DOD is a fundamental parameter for quantifying dust radiative effects and their impacts on solar energy generation, making accurate DOD simulation essential for both climate modeling and renewable energy applications. Figure 8 presents a comprehensive assessment of DOD simulation performance across six dust models covering the dust belt region (30° W-115° E, 0°-50° N).

https://doi.org/10.5194/essd-2025-628
Preprint. Discussion started: 24 March 2026

The spatial distribution of DOD biases reveals widespread systematic underestimation across all models, though magnitudes and spatial patterns vary (Fig. 8a-f). The iDust_CTRL configuration exhibits pronounced regional imbalances, with notable positive biases in the Gobi Desert contrasting with widespread negative biases across other dust source areas. Both iDust_ut and iDust_ut_adpt configurations alleviate the systematic overestimation in the Gobi region. Among comparison models, CAMS shows localized positive biases in portions of North Africa alongside general underestimation elsewhere, while EAC4 exhibits even more pronounced positive biases in the Gobi region than iDust_CTRL. MERRA-2 presents the most spatially uniform bias distribution, though underestimating DOD across the Arabian Peninsula. These spatial patterns demonstrate that regional bias imbalances remain a pervasive challenge in forecast and reanalysis products.

Correlation analysis (Fig. 8g) reveals that reanalysis products exhibit superior performance in capturing DOD spatiotemporal variations, with EAC4 achieving a correlation coefficient of 0.73 and MERRA-2 achieving 0.64. The three iDust configurations share identical correlation coefficients of 0.61. CAMS exhibits the lowest correlation at 0.55, indicating limitations in capturing dust spatiotemporal variability. Mean absolute error analysis (Fig. 8h) reveals relatively consistent performance across model categories, with forecast models maintaining MAE values of 0.15 while reanalysis products achieve marginally better performance at 0.13.

The Threat Score analysis (Fig. 8i-j) reveals pronounced differences in the ability of models to detect dust events of varying intensities. For moderate dust events with DOD values between 0.5 and 1.0, reanalysis products demonstrate superior detection capabilities, with MERRA-2 achieving 18.31 % and EAC4 reaching 17.75 %. The iDust configurations show comparable performance around 12-14 %, while CAMS shows the lowest TS at 10.54 %. Performance disparities become particularly significant for extreme dust events exceeding the DOD values of 1.0. Implementation of the iDust-ut dataset yields substantial improvements in simulation capability. The iDust_ut_adpt configuration achieves the highest Threat Score at 10.70 %, representing a 47 % enhancement compared to the control configuration's 7.28 %. The iDust_ut configuration shows intermediate improvement at 9.84 %. These optimized configurations surpass both EAC4 (8.43 %) and MERRA-2 (7.07 %) reanalysis products in extreme DOD simulation. CAMS achieves a Threat Score of 2.61 % for extreme dust events, indicating limitations in detecting high-intensity dust storms in this region.

In summary, incorporating the iDust-ut dataset delivers consistent improvements across diverse dust metrics and spatial scales. The enhanced performance in extreme event simulation is particularly significant for operational applications, where accurate forecasting of high-intensity dust events remains critical for impact mitigation. The optimized iDust configurations achieve performance levels that match or exceed those of reanalysis products in specific metrics, demonstrating that accurate representation of physical processes remains fundamental to effective dust modeling. However, the systematic underestimation of DOD observed across all evaluated models indicates persistent challenges in dust emission and optical property parameterizations requiring continued research. Nevertheless, the substantial improvements achieved through the

https://doi.org/10.5194/essd-2025-628
Preprint. Discussion started: 24 March 2026

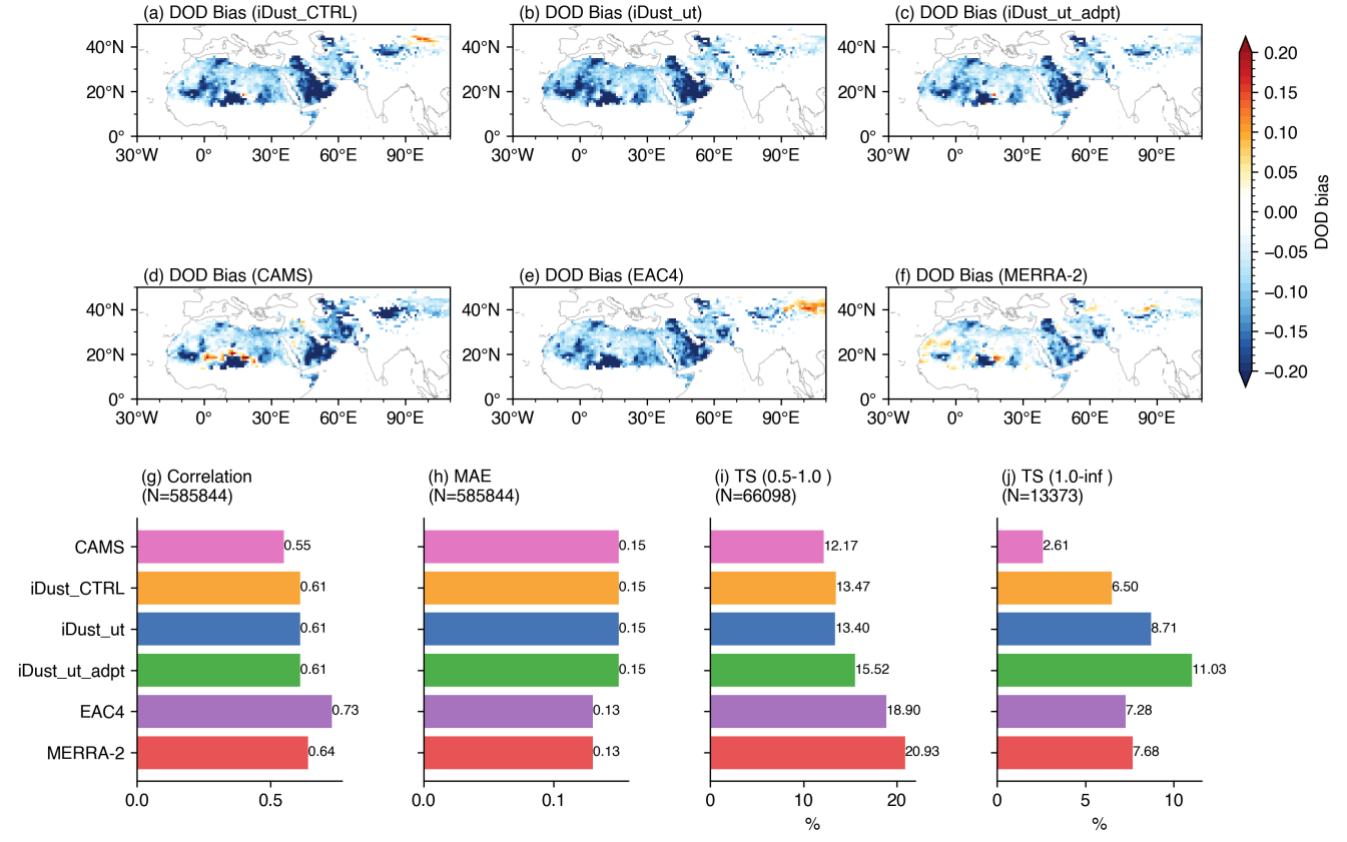

Figure 8. Evaluation of dust source DOD simulation performance across different models in the dust belt region (30°W-110°E, 0°-50°N). (a-f) Spatial distribution of DOD biases for different models. (g-j) Statistical performance metrics for each model in the dust belt region, including correlation coefficients, Mean Absolute Error (MAE), and Threat Scores for moderate-intensity dust events (0.5<DOD<1) and extreme dust events (DOD>1.0).

6. Discussion

6.1 Advantages

Multi-source data constraint reduces uncertainties. By integrating ground observations, satellite remote sensing data, and multiple reanalysis datasets, this study significantly reduces uncertainties in u_t estimation. The multi-source data fusion strategy effectively compensates for the inherent limitations of individual data sources, providing objective and reliable constraints for key algorithm parameters. The adaptive τ_t determination algorithm compensates for systematic biases across different reanalysis datasets, substantially reducing the reanalysis-dependent uncertainty. The resulting iDust-ut dataset demonstrates strong consistency with field observations (r=0.93, MAE=0.80 m s^{-1}).

https://doi.org/10.5194/essd-2025-628
Preprint. Discussion started: 24 March 2026

Effective wind speed adaptation scheme. The u_t adaptation algorithm compensates for regional wind speed biases, effectively mitigating dust emission simulation errors caused by systematic surface wind speed biases. Implementing adaptive u_t enhances the capability for forecasting extreme dust events, achieving a 15 % improvement in Threat Score for extreme PM_{10} events in Northwestern China and a 21 % improvement in Threat Score for extreme DOD events in the dust belt compared to the unadapted scheme. Validation results based on multi-year wind speed samples demonstrate temporal consistency of the adaptation scheme, confirming its reliability for long-term operational applications.

Enhanced operational forecasting efficiency. The iDust-ut dataset offers an efficient solution for enhancing dust forecast accuracy without requiring additional computational resources, making it particularly suitable for operational forecasting systems requiring timely predictions. Implementation requires only simple threshold replacement, avoiding the complexity of modifying emission schemes or recalibrating multiple parameters.

6.2 Uncertainties and Limitations

Observational constraints in remote regions. Ground-based meteorological observations remain sparse across vast desert interiors, particularly in the Eastern Sahara, the Arabian Peninsula, and the interior of Australia. Rigorous quality control criteria, while essential for ensuring reliable u_t estimates, further reduce the number of usable stations in these data-sparse regions. Threshold uncertainties arise from two primary sources. First, limited station density in remote areas necessitates greater reliance on satellite-based interpolation methods. Second, regions with infrequent dust emissions provide fewer statistical samples for threshold determination, even when observation stations are present. The uncertainty quantification in Figure 4a reflects both factors, with the highest uncertainties typically occurring in regions that combine sparse observations with low dust emission frequencies. As global observation networks expand and accumulate longer temporal records, both spatial coverage and statistical robustness will improve, progressively reducing these uncertainties.

Methodological Assumptions and Their Implications. The indirect constraint method assumes that τ_t exhibits better spatial continuity than u_t, enabling more reliable interpolation between stations. This assumption is generally valid given that column-integrated atmospheric optical properties vary more smoothly than surface characteristics. However, sharp transitions in aerosol composition, topographic barriers, or localized emission sources can create discontinuities that challenge this assumption. Additionally, the threshold adaptation scheme assumes that systematic biases in reanalysis wind speeds can be adequately compensated through linear scaling of u_t values. While effective for mean conditions, this linear adjustment may not fully capture nonlinear wind speed biases that occur during extreme wind events or in complex terrain. The global scaling coefficient derived in Sect. 3.3 represents an average correction that may over- or under-compensate in specific meteorological conditions. Future developments could address these limitations through nonlinear adjustment

https://doi.org/10.5194/essd-2025-628
Preprint. Discussion started: 24 March 2026

660 schemes that account for wind speed-dependent biases. The integration of machine learning approaches may also help capture complex relationships between multiple environmental variables and threshold values.

7. Data Availability

The global 1°×1° monthly iDust-ut dataset is publicly available on the Zenodo platform, accessible at https://zenodo.org/doi/10.5281/zenodo.15580883 (Chong and Chen, 2026). The dataset includes iDust-ut data along with
665 model-adaptive datasets based on 2023 wind speeds from iDust, and 2020-2024 wind speeds from CAMS and MERRA-2. All datasets are released under the Creative Commons Attribution 4.0 International License (CC BY 4.0), allowing free access and usage.

The Integrated Surface Database (ISD) data is available at https://www.ncei.noaa.gov/data/global-hourly/archive/csv/;
670 MODIS aerosol products can be downloaded from https://ladsweb.modaps.eosdis.nasa.gov/archive/allData/61/; VIIRS aerosol products are accessible via https://ladsweb.modaps.eosdis.nasa.gov/archive/allData/5200/; ERA5 reanalysis data is sourced from https://cds.climate.copernicus.eu/datasets/reanalysis-era5-single-levels; MERRA-2 datasets are available at https://disc.gsfc.nasa.gov/datasets/; CAMS global atmospheric composition forecasts can be accessed through https://ads.atmosphere.copernicus.eu/datasets/cams-global-atmospheric-composition-forecasts; EAC4 reanalysis data is
675 available from https://ads.atmosphere.copernicus.eu/datasets/cams-global-reanalysis-eac4.

8. Code Availability

The complete code for generating the iDust-ut dataset is available at https://zenodo.org/doi/10.5281/zenodo.15580883 (Chong and Chen, 2026). The codebase includes core modules for the DuTS algorithm implementation, global u_t calculation, model u_t adapation. For any inquiries regarding the dataset or code, please contact Xi Chen at chenxi@lasg.iap.ac.cn.

680 **9. Conclusions**

This study develops a high-precision global dust emission threshold wind speed dataset (iDust-ut) and an adaptation algorithm to compensate for model wind speed bias, advancing global dust forecasting capabilities. The research establishes a station-level u_t determination method by optimizing the Dust Emission Threat Score (DuTS) based on ISD ground observations. These station values are then integrated with satellite remote sensing and reanalysis data to derive a global
685 gridded u_t field, significantly reducing the dependence of u_t estimation on reanalysis data. Additionally, a model-adaptive u_t adjustment scheme is developed to compensate for systematic wind speed biases in numerical models.

https://doi.org/10.5194/essd-2025-628
Preprint. Discussion started: 24 March 2026

Validation against field observations demonstrates high dataset accuracy (r=0.93, MAE=0.8 m s^{-1}). Application evaluation in the iDust model shows that this dataset substantially improves dust forecasting performance. Compared to existing products such as CAMS, MERRA-2, EAC4, and iDust simulations using constant u_t, the iDust model implementing the iDust-ut dataset demonstrates notable advantages in both PM_{10} and DOD simulations, particularly achieving 108 % improvement in forecasting extreme PM_{10} events in Northwestern China. Furthermore, implementing this dataset requires minimal additional computational resources, making it highly suitable for operational forecasting.

This research provides a high-quality foundational dataset for global numerical dust forecasting. Through multi-source data fusion and innovation adaptive algorithm, it effectively enhances forecast accuracy of dust models. The dataset has been publicly released on Zenodo (Chong and Chen, 2026) in standard NetCDF format, facilitating straightforward integration into existing modeling frameworks. The iDust-ut dataset can be directly implemented in various dust emission schemes that utilize 10-meter wind speed. The model-adaptive algorithm requires only multiplying the base threshold by model-specific scaling factors derived from wind speed statistics. This computationally efficient approach enables seamless adoption across diverse modeling platforms, from global climate models and regional weather prediction systems to specialized dust forecasting applications, without requiring fundamental modifications to existing model architectures.

Author contribution

X.C. supervised the research. M.C. and S.W. conceived the data processing framework. M.C. and X.C. developed the dataset algorithm and designed the experiments. Y.L. (Yuan Liang), S.-J.L., and Z.L. contributed to model optimization and compilation. B.P. provided methodological guidance and reference datasets for validation. Y.L. (Yimin Liu) provided scientific guidance and contributed to the manuscript preparation. M.C. wrote the initial draft of the manuscript. All authors participated in manuscript revision and approved the final version.

Competing interests

The authors declare that they have no conflict of interest.

Acknowledgements

The authors sincerely acknowledge the editor and reviewers for their constructive comments and suggestions. The authors are grateful to all data providers whose data have been used in this study. This research is supported by the National Natural

https://doi.org/10.5194/essd-2025-628
Preprint. Discussion started: 24 March 2026

Science Foundation of China (42288101, 42275174) and the National Key R&D Program of China (2022YFF0802000, 2022YFF0802001, 2024YFB4204800). The authors also thank the Earth System Science Numerical Simulator Facility (EarthLab), the Super Computing Network (SCNet), and HPC department of Sugon Beijing for their support during the development.

References

Allen, C. J. T., Washington, R., and Engelstaedter, S.: Dust emission and transport mechanisms in the central Sahara: Fennec ground-based observations from Bordj Badji Mokhtar, June 2011, J. Geophys. Res. Atmospheres, 118, 6212–6232, https://doi.org/10.1002/jgrd.50534, 2013.

AlNasser, F., Chehbouni, A., and Entekhabi, D.: Influences of soil moisture and vegetation cover on dust emission using satellite observations, Aeolian Res., 72, 100961, https://doi.org/10.1016/j.aeolia.2025.100961, 2025.

Anderson, T. L., Wu, Y., Chu, D. A., Schmid, B., Redemann, J., and Dubovik, O.: Testing the MODIS satellite retrieval of aerosol fine-mode fraction, J. Geophys. Res. Atmospheres, 110, 2005JD005978, https://doi.org/10.1029/2005JD005978, 2005.

Cakmur, R. V., Miller, R. L., and Torres, O.: Incorporating the effect of small-scale circulations upon dust emission in an atmospheric general circulation model, J. Geophys. Res. Atmospheres, 109, 2003JD004067, https://doi.org/10.1029/2003JD004067, 2004.

Chen, X., Chong, M., Lin, S., Liang, Z., Ginoux, P., Liang, Y., Zhang, B., Song, Q., Wang, S., Li, J., and Liu, Y.: The Efficient Integration of Dust and Numerical Weather Prediction for Renewable Energy Applications, J. Adv. Model. Earth Syst., 17, e2024MS004525, https://doi.org/10.1029/2024MS004525, 2025.

Chong, M. and Chen, X.: iDust-ut: A Global Wind Erosion Threshold Dataset for Enhanced Dust Forecasting (1.4), https://doi.org/10.5281/ZENODO.15580883, 2026.

CNEMC: PM10, 2025.

Darmenova, K., Sokolik, I. N., Shao, Y., Marticorena, B., and Bergametti, G.: Development of a physically based dust emission module within the Weather Research and Forecasting (WRF) model: Assessment of dust emission parameterizations and input parameters for source regions in Central and East Asia, J. Geophys. Res. Atmospheres, 114, 2008JD011236, https://doi.org/10.1029/2008JD011236, 2009.

Draxler, R. R., Ginoux, P., and Stein, A. F.: An empirically derived emission algorithm for wind-blown dust, J. Geophys. Res. Atmospheres, 115, 2009JD013167, https://doi.org/10.1029/2009JD013167, 2010.

Faber, E., Rocha-Lima, A., Colarco, P., and Baker, B.: Evaluation of 10-m Wind Speed From ISD Meteorological Stations and the MERRA-2 Reanalysis: Impacts on Dust Emission in the Arabian Peninsula, J. Geophys. Res. Atmospheres, 129, e2024JD040885, https://doi.org/10.1029/2024JD040885, 2024.

Gaspari, G. and Cohn, S. E.: Construction of correlation functions in two and three dimensions, Q. J. R. Meteorol. Soc., 125, 723–757, https://doi.org/10.1002/qj.49712555417, 1999.

https://doi.org/10.5194/essd-2025-628
Preprint. Discussion started: 24 March 2026

Gelaro, R., McCarty, W., Suárez, M. J., Todling, R., Andrea Molod, Takacs, L., Randles, C. A., Darmenov, A., Bosilovich, M. G., Reichle, R., Wargan, K., Coy, L., Cullather, R., Draper, C., Akella, S., Buchard, V., Conaty, A., Da Silva, A. M., Gu, W., Kim, G.-K., Koster, R., Lucchesi, R., Merkova, D., Nielsen, J. E., Partyka, G., Pawson, S., Putman, W., Rienecker, M., Schubert, S. D., Sienkiewicz, M., and Zhao, B.: The Modern-Era Retrospective Analysis for Research and Applications, Version 2 (MERRA-2), J. Clim., 30, 5419–5454, https://doi.org/10.1175/JCLI-D-16-0758.1, 2017.

Ginoux, P. and Deroubaix, A.: Space Observations of Dust in East Asia, in: Air Pollution in Eastern Asia: An Integrated Perspective, edited by: Bouarar, I., Wang, X., and Brasseur, G. P., Springer International Publishing, Cham, 365–383, https://doi.org/10.1007/978-3-319-59489-7_17, 2017.

Ginoux, P., Chin, M., Tegen, I., Prospero, J. M., Holben, B., Dubovik, O., and Lin, S.: Sources and distributions of dust aerosols simulated with the GOCART model, J. Geophys. Res. Atmospheres, 106, 20255–20273, https://doi.org/10.1029/2000JD000053, 2001.

Hao, Y., Wang, Z., Xue, L., Lou, S., Ding, K., Qin, Y., and Huang, X.: Modeling the Effects of Vegetation and Snow on Dust Storm Over the Gobi Desert, J. Geophys. Res. Atmospheres, 129, e2024JD041407, https://doi.org/10.1029/2024JD041407, 2024.

Heinold, B., Helmert, J., Hellmuth, O., Wolke, R., Ansmann, A., Marticorena, B., Laurent, B., and Tegen, I.: Regional modeling of Saharan dust events using LM-MUSCAT: Model description and case studies, J. Geophys. Res. Atmospheres, 112, 2006JD007443, https://doi.org/10.1029/2006JD007443, 2007.

Hennen, M., Chappell, A., Webb, N. P., Schepanski, K., Baddock, M. C., Eckardt, F. D., Kandakji, T., Lee, J. A., Nobakht, M., and Von Holdt, J.: A new framework for evaluating dust emission model development using dichotomous satellite observations of dust emission, Sci. Total Environ., 912, 169237, https://doi.org/10.1016/j.scitotenv.2023.169237, 2024.

Hersbach, H., Bell, B., Berrisford, P., Hirahara, S., Horányi, A., Muñoz-Sabater, J., Nicolas, J., Peubey, C., Radu, R., Schepers, D., Simmons, A., Soci, C., Abdalla, S., Abellan, X., Balsamo, G., Bechtold, P., Biavati, G., Bidlot, J., Bonavita, M., De Chiara, G., Dahlgren, P., Dee, D., Diamantakis, M., Dragani, R., Flemming, J., Forbes, R., Fuentes, M., Geer, A., Haimberger, L., Healy, S., Hogan, R. J., Hólm, E., Janisková, M., Keeley, S., Laloyaux, P., Lopez, P., Lupu, C., Radnoti, G., De Rosnay, P., Rozum, I., Vamborg, F., Villaume, S., and Thépaut, J.: The ERA5 global reanalysis, Q. J. R. Meteorol. Soc., 146, 1999–2049, https://doi.org/10.1002/qj.3803, 2020.

Hsu, N. C., Jeong, M. -J., Bettenhausen, C., Sayer, A. M., Hansell, R., Seftor, C. S., Huang, J., and Tsay, S. -C.: Enhanced Deep Blue aerosol retrieval algorithm: The second generation, J. Geophys. Res. Atmospheres, 118, 9296–9315, https://doi.org/10.1002/jgrd.50712, 2013.

IEA: World Energy Investment 2024, IEA, 2024.

Inness, A., Ades, M., Agustí-Panareda, A., Barré, J., Benedictow, A., Blechschmidt, A.-M., Dominguez, J. J., Engelen, R., Eskes, H., Flemming, J., Huijnen, V., Jones, L., Kipling, Z., Massart, S., Parrington, M., Peuch, V.-H., Razinger, M., Remy, S., Schulz, M., and Suttie, M.: The CAMS reanalysis of atmospheric composition, Atmospheric Chem. Phys., 19, 3515–3556, https://doi.org/10.5194/acp-19-3515-2019, 2019.

Klose, M., Gill, T. E., Etyemezian, V., Nikolich, G., Ghodsi Zadeh, Z., Webb, N. P., and Van Pelt, R. S.: Dust emission from crusted surfaces: Insights from field measurements and modelling, Aeolian Res., 40, 1–14, https://doi.org/10.1016/j.aeolia.2019.05.001, 2019.

https://doi.org/10.5194/essd-2025-628
Preprint. Discussion started: 24 March 2026

Kong, K., Nandintsetseg, B., Shinoda, M., Ishizuka, M., Kurosaki, Y., Bat-Oyun, T., and Gantsetseg, B.: Seasonal variations in threshold wind speed for saltation depending on soil temperature and vegetation: A case study in the Gobi Desert, Aeolian Res., 52, 100716, https://doi.org/10.1016/j.aeolia.2021.100716, 2021.

Kurosaki, Y. and Mikami, M.: Threshold wind speed for dust emission in east Asia and its seasonal variations, J. Geophys. Res. Atmospheres, 112, 2006JD007988, https://doi.org/10.1029/2006JD007988, 2007.

Leung, D. M., Kok, J. F., Li, L., Okin, G. S., Prigent, C., Klose, M., Pérez García-Pando, C., Menut, L., Mahowald, N. M., Lawrence, D. M., and Chamecki, M.: A new process-based and scale-aware desert dust emission scheme for global climate models – Part I: Description and evaluation against inverse modeling emissions, Atmospheric Chem. Phys., 23, 6487–6523, https://doi.org/10.5194/acp-23-6487-2023, 2023.

Marticorena, B. and Bergametti, G.: Modeling the atmospheric dust cycle: 1. Design of a soil-derived dust emission scheme, J. Geophys. Res. Atmospheres, 100, 16415–16430, https://doi.org/10.1029/95JD00690, 1995.

Masoom, A., Kosmopoulos, P., Bansal, A., Gkikas, A., Proestakis, E., Kazadzis, S., and Amiridis, V.: Forecasting dust impact on solar energy using remote sensing and modeling techniques, Sol. Energy, 228, 317–332, https://doi.org/10.1016/j.solener.2021.09.033, 2021.

Suomi National Polar-orbiting Partnership | NASA's Earth Observing System: https://eospso.nasa.gov/missions/suomi-national-polar-orbiting-partnership, last access: 13 October 2025.

Joint Polar Satellite System-1 | NASA's Earth Observing System: https://eospso.nasa.gov/missions/joint-polar-satellite-system-1, last access: 13 October 2025.

MODIS Web: https://modis.gsfc.nasa.gov/about/specifications.php, last access: 13 October 2025.

Nelli, N., Francis, D., Sow, M., Fonseca, R., Alkatheeri, A., Bosc, E., and Bergametti, G.: The Wind-Blown Sand Experiment in the Empty Quarter Desert: Roughness Length and Saltation Characteristics, Earth Space Sci., 11, e2024EA003512, https://doi.org/10.1029/2024EA003512, 2024.

Notaro, M., Yu, Y., and Kalashnikova, O. V.: Regime shift in Arabian dust activity, triggered by persistent Fertile Crescent drought, J. Geophys. Res. Atmospheres, 120, https://doi.org/10.1002/2015JD023855, 2015.

Panat, S. and Varanasi, K. K.: Electrostatic dust removal using adsorbed moisture–assisted charge induction for sustainable operation of solar panels, Sci. Adv., 8, eabm0078, https://doi.org/10.1126/sciadv.abm0078, 2022.

Pitkänen, M. R. A., Arola, A., Bennouna, Y., Benedictow, A., Blake, L., Bouarar, I., Cuevas, E., Errera, Q., Eskes, H. J., Griesfeller, J., Basart, S., Kapsomenakis, J., Langerock, B., Mortier, A., Pison, I., Ramonet, M., Richter, A., Schoenhardt, A., Schulz, M., Tarniewicz, J., Thouret, V., Tsikerdekis, A., Warneke, T., and Zerefos, C.: Validation report of the CAMS near-real-time global atmospheric composition service Period March – May 2023, https://doi.org/10.24380/AC0R-AO9U, 2023.

Platnick, S.: MODIS Atmosphere L3 Monthly Product, 2015.

Pu, B. and Ginoux, P.: How reliable are CMIP5 models in simulating dust optical depth?, Atmospheric Chem. Phys., 18, 12491–12510, https://doi.org/10.5194/acp-18-12491-2018, 2018.

Pu, B., Ginoux, P., Guo, H., Hsu, N. C., Kimball, J., Marticorena, B., Malyshev, S., Naik, V., O'Neill, N. T., Pérez García-Pando, C., Paireau, J., Prospero, J. M., Shevliakova, E., and Zhao, M.: Retrieving the global distribution of the threshold of

wind erosion from satellite data and implementing it into the Geophysical Fluid Dynamics Laboratory land–atmosphere model (GFDL AM4.0/LM4.0), Atmospheric Chem. Phys., 20, 55–81, https://doi.org/10.5194/acp-20-55-2020, 2020.

Ramon, J., Lledó, L., Torralba, V., Soret, A., and Doblas-Reyes, F. J.: What global reanalysis best represents near-surface winds?, Q. J. R. Meteorol. Soc., 145, 3236–3251, https://doi.org/10.1002/qj.3616, 2019.

Randles, C. A., da Silva, A. M., Buchard, V., Colarco, P. R., Darmenov, A., Govindaraju, R., Smirnov, A., Holben, B., Ferrare, R., Hair, J., Shinozuka, Y., and Flynn, C. J.: The MERRA-2 Aerosol Reanalysis, 1980 Onward. Part I: System Description and Data Assimilation Evaluation, J. Clim., 30, 6823–6850, https://doi.org/10.1175/JCLI-D-16-0609.1, 2017.

Rémy, S., Kipling, Z., Flemming, J., Boucher, O., Nabat, P., Michou, M., Bozzo, A., Ades, M., Huijnen, V., Benedetti, A., Engelen, R., Peuch, V.-H., and Morcrette, J.-J.: Description and evaluation of the tropospheric aerosol scheme in the European Centre for Medium-Range Weather Forecasts (ECMWF) Integrated Forecasting System (IFS-AER, cycle 45R1), Geosci Model Dev, 12, 4627–4659, https://doi.org/10.5194/gmd-12-4627-2019, 2019.

Rémy, S., Kipling, Z., Huijnen, V., Flemming, J., Nabat, P., Michou, M., Ades, M., Engelen, R., and Peuch, V.-H.: Description and evaluation of the tropospheric aerosol scheme in the Integrated Forecasting System (IFS-AER, cycle 47R1) of ECMWF, Geosci. Model Dev., 15, 4881–4912, https://doi.org/10.5194/gmd-15-4881-2022, 2022.

Sayer, A. M., Hsu, N. C., Bettenhausen, C., and Jeong, M. -J.: Validation and uncertainty estimates for MODIS Collection 6 “Deep Blue” aerosol data, J. Geophys. Res. Atmospheres, 118, 7864–7872, https://doi.org/10.1002/jgrd.50600, 2013.

Scherllin-Pirscher, B., Nickovic, S., Votsis, A., Cvetkovic, B., Amiridis, V., Bolic, T., Brenot, H., Brock, G., Clarkson, R. J., Durant, A., Hirtl, M., Lekas, T. I., Mona, L., Nasser, H., Ryder, C. L., Ryuzaki, J., Suárez-Molina, D., Vukovic Vimic, A., and Basart, S.: Airborne Soil-Derived Dust Hazards in Aviation, Bull. Am. Meteorol. Soc., 106, E125–E145, https://doi.org/10.1175/BAMS-D-23-0311.1, 2025.

Smith, A., Lott, N., and Vose, R.: The Integrated Surface Database: Recent Developments and Partnerships, Bull. Am. Meteorol. Soc., 92, 704–708, https://doi.org/10.1175/2011BAMS3015.1, 2011.

Stout, J. E. and Arimoto, R.: Threshold wind velocities for sand movement in the Mescalero Sands of southeastern New Mexico, J. Arid Environ., 74, 1456–1460, https://doi.org/10.1016/j.jaridenv.2010.05.011, 2010.

VIIRS Atmosphere Science Team, S.: VIIRS/NOAA20 Deep Blue Level 3 daily aerosol data, 1 degree x1 degree grid, https://doi.org/10.5067/VIIRS/AERDB_D3_VIIRS_NOAA20.002, 2023a.

VIIRS Atmosphere Science Team, S.: VIIRS/SNPP Deep Blue Level 3 daily aerosol data, 1 degree x1 degree grid, https://doi.org/10.5067/VIIRS/AERDB_D3_VIIRS_SNPP.002, 2023b.

Xi, X.: Revisiting the Recent Dust Trends and Climate Drivers Using Horizontal Visibility and Present Weather Observations, J. Geophys. Res., 126, e2021JD034687, https://doi.org/10.1029/2021JD034687, 2021.

Yang, X., He, Q., Matimin, A., Yang, F., Huo, W., Liu, X., Zhao, T., and Shen, S.: Threshold Velocity for Saltation Activity in the Taklimakan Desert, Pure Appl. Geophys., 174, 4459–4470, https://doi.org/10.1007/s00024-017-1644-5, 2017.

Zhang, C., Yan, M., Du, H., Ban, J., Chen, C., Liu, Y., and Li, T.: Mortality risks from a spectrum of causes associated with sand and dust storms in China, Nat. Commun., 14, 6867, https://doi.org/10.1038/s41467-023-42530-w, 2023.

https://doi.org/10.5194/essd-2025-628
Preprint. Discussion started: 24 March 2026

Zhou, C., Zhang, X., Zhang, J., and Zhang, X.: Representations of dynamics size distributions of mineral dust over East Asia by a regional sand and dust storm model, Atmospheric Res., 250, 105403, https://doi.org/10.1016/j.atmosres.2020.105403, 2021.

860

https://doi.org/10.5194/essd-2025-628
Preprint. Discussion started: 24 March 2026

Appendix

Appendix A. Dataset Details

Table A1. Dust-related Present Weather Codes in the ISD Dataset

Present Weather Code	Dust code definition
06	Widespread dust in suspension in the air, not raised by wind at or near the station at the time of observation
07	Dust or sand raised by wind at or near the station at the time of observation, but no well-developed dust whirl(s) or sand whirl(s), and no dust storm or sandstorm seen or, in the case of ships, blowing spray at the station
08	Well developed dust whirl(s) or sand whirl(s) seen at or near the station during the preceding hour or at the time of observation, but no dust storm or sandstorm
09	Dust storm or sandstorm within sight at the time of observation, or at the station during the preceding hour
30	Slight or moderate dust storm or sandstorm has decreased during the preceding hour
31	Slight or moderate dust storm or sandstorm no appreciable change during the preceding hour
32	Slight or moderate dust storm or sandstorm has begun or has increased during the preceding hour
33	Severe dust storm or sandstorm has decreased during the preceding hour
34	Severe dust storm or sandstorm no appreciable change during the preceding hour
35	Severe dust storm or sandstorm has begun or has increased during the preceding hour
98	Thunderstorm combined with duststorm or sandstorm at time of observation, thunderstorm at time of observation

https://doi.org/10.5194/essd-2025-628
Preprint. Discussion started: 24 March 2026

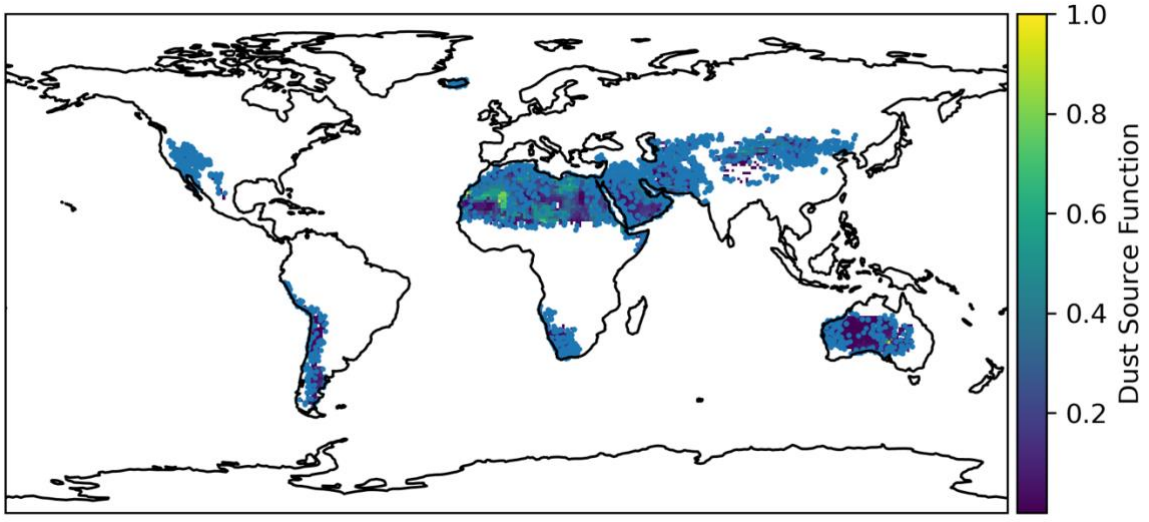

Figure A1. Dust source regions at 1° resolution (Ginoux et al., 2001) and locations of ISD stations within 1° buffer zones of the dust sources.

Table A2. Field campaign u_t values

Station name	Longitude	Latitude	Observation Period	Mean u_t	Reference
Bordj Badji Mokhtar	0.92° E	21.38° N	June 2011	8 m s^{-1}	(Allen et al., 2013)
Near Field	103.799° W	32.378° N	8 April to 29 July 2005	10.8 m s^{-1}	(Stout and Arimoto, 2010)
Gnome site	103.88° W	32.266° N	8 April to 29 July 2005	10.5 m s^{-1}	(Stout and Arimoto, 2010)
TaZhong	83.66° E	38.98° N	1 August 2008 to 31 July 2009	5.9 m s^{-1}	(Yang et al., 2017)
WISE-UAE	53.72° E	23.576° N	September 2022 to February 2023	7.7 m s^{-1}	(Nelli et al., 2024)

Appendix B. Gaspari-Cohn Localization Function

The Gaspari-Cohn localization function is a compactly supported fifth-order polynomial function with the expression:

$$R^{GC}(r) = \begin{cases} -\frac{1}{4}r^5 + \frac{1}{2}r^4 + \frac{5}{8}r^3 - \frac{5}{3}r^2 + 1, & 0 \le r \le 1 \\ \frac{1}{12}r^5 - \frac{1}{2}r^4 + \frac{5}{8}r^3 + \frac{5}{3}r^2 - 5r + 4 - \frac{2}{3}r^{-1}, & 1 \le r \le 2 \\ 0, & r \ge 2 \end{cases},$$

https://doi.org/10.5194/essd-2025-628
Preprint. Discussion started: 24 March 2026

Open Access Earth System Science Data Discussions

where $r = \frac{d}{R_{loc}}$ is the normalized distance, with d being the distance from the grid point to the station, and R_{loc} being the localization radius. The distance from grid point to station is calculated using the haversine formula:

$$d = 2r\ arcsin\left(\sqrt{sin^2\frac{\Delta\phi}{2} + cos\phi_1 cos\phi_2 sin^2\frac{\Delta\theta}{2}}\right),$$

where r=6371 km is the Earth's radius, φ_1 and φ_2 are the latitudes of the grid point and station respectively, $\Delta\varphi = \varphi_1 - \varphi_2$. θ_1 and θ_2 are the longitudes of the grid point and station respectively, and $\Delta\theta = \theta_1 - \theta_2$.

Appendix C. Method for Calculating PM_{10} from Dust Concentration

For CAMS and EAC4 reanalysis products, dust PM_{10} is calculated as:

$$PM_{10,dust} = \rho_a \times (DD1 + DD2 + DD3 \times 0.4),$$

where DD1, DD2, and DD3 are the mass mixing ratios (kg kg^{-1}) of dust particles with radii of 0.03-0.55 μm, 0.55-0.9 μm, and 0.9-20 μm respectively, and ρ_a is the surface air density, assumed to be 1.29 kg m^{-3}.

For MERRA-2 and iDust models, dust PM_{10} is calculated as:

$$PM_{10,dust} = \rho_a \times (DD1 + DD2 + DD3 + DD4 \times 0.74),$$

where DD1, DD2, DD3, and DD4 are the mass mixing ratios (kg kg^{-1}) of dust particles with radii of 0.1-1.0 μm, 1.0-1.8 μm, 1.8-3.0 μm (2.0-3.0 μm for iDust), and 3.0-6.0 μm respectively.

Appendix D. Statistical Metric Calculation Methods

(1) Pearson Correlation Coefficient (r):

$$r = \frac{\sum_{t=1}^{n}(O_t - \bar{O})(M_t - \bar{M})}{\sum_{t=1}^{n}(O_t - \bar{O})^2 \sum_{t=1}^{n}(M_t - \bar{M})^2},$$

where O_t and M_t represent the observed and modeled values at time t respectively, $\bar{O}$ and $\bar{M}$ represent the mean values of observations and model respectively, and n is the total number of samples.

(2) Mean Absolute Error (MAE):

$$MAE = \frac{1}{n}\sum_{t=1}^{n} | M_t - O_t |.$$

(3) Threat Score (TS):

$$TS = \frac{a}{a+b+c},$$

https://doi.org/10.5194/essd-2025-628
Preprint. Discussion started: 24 March 2026

where a is the number of hits (both observations and simulations are within the threshold range), b is the number of false alarms (model is within threshold range but observations are not), and c is the number of misses (observations are within threshold range but model is not).

(4) Point-Biserial Correlation:

$$r_{pb} = \frac{\overline{X_1} - \overline{X_0}}{S_x} \sqrt{\frac{n_1 n_0}{n(n-1)}},$$

where:

$\overline{X_1}$: mean of continuous variable X when binary variable Y=1,

$\overline{X_0}$: mean of continuous variable X when binary variable Y=0,

S_x: standard deviation of continuous variable X,

n_1: number of samples where Y=1,

n_0: number of samples where Y=0,

N: total number of samples ($n = n_1 + n_0$).